Menefee Anne Holland (Orcid ID: 0000-0003-2740-3208)
Welch Nathan J. (Orcid ID: 0000-0002-8416-6803)
Frash Luke P. (Orcid ID: 0000-0002-5424-4698)
Carey James William (Orcid ID: 0000-0001-8488-2925)
Ellis Brian R. (Orcid ID: 0000-0002-7253-4285)

Rapid mineral precipitation during shear fracturing of carbonate-rich shales

Anne H. Menefee,[1] Nathan J. Welch,[2] Luke P. Frash, [2] Wes Hicks,[3] J. William Carey, [2] and Brian R. Ellis[1,4*]

1. Department of Civil and Environmental Engineering
University of Michigan, Ann Arbor, MI, United States

2. Earth & Environmental Sciences, Los Alamos National Laboratory
Los Alamos, NM, United States

3. Design Engineering & Technology, Los Alamos National Laboratory
Los Alamos, NM, United States

4. ORISE at the National Energy Technology Laboratory
Morgantown, WV, United States

*Corresponding author

Abstract

Target subsurface reservoirs for emerging low-carbon energy technologies and geologic carbon sequestration typically have low permeability and thus rely heavily on fluid transport through natural and induced fracture networks. Sustainable development of these systems requires deeper understanding of how geochemically mediated deformation impacts fracture microstructure and permeability evolution, particularly with respect to geochemical reactions between pore fluids and the host rock. In this work, a series of triaxial direct shear experiments was designed to evaluate how fractures generated at subsurface conditions respond to penetration of reactive fluids with a focus on the role of mineral precipitation. Calcite-rich shale cores were directly sheared under 3.5 MPa confining pressure using $BaCl_2$-rich solutions as a working fluid. Experiments were conducted within an x-ray computed tomography (xCT) scanner to capture 4D evolution of fracture geometry and precipitate growth. Three shear tests evidenced non-uniform

This is the author manuscript accepted for publication and has undergone full peer review but has not been through the copyediting, typesetting, pagination and proofreading process, which may lead to differences between this version and the Version of Record. Please cite this article as doi: 10.1029/2019JB018864

precipitation of barium carbonates ($BaCO_3$) along through-going fractures, where the extent of precipitation increased with increasing calcite content. Precipitates were strongly localized within fracture networks due to mineral, geochemical, and structural heterogeneities and generally concentrated in smaller apertures where rock:water ratios were highest. The combination of elevated fluid saturation and reactive surface area created in freshly activated fractures drove near-immediate mineral precipitation that led to an 80% permeability reduction and significant flow obstruction in the most reactive core. While most previous studies have focused on mixing-induced precipitation, this work demonstrates that fluid-rock interactions can trigger precipitation-induced permeability alterations that can initiate or mitigate risks associated with subsurface energy systems.

1. Introduction

The subsurface currently provides roughly 80% of national energy demands and is primed to play a critical role in the development of low-carbon energy systems and the mitigation of climate change (Pyrak-Nolte et al., 2015). Target reservoirs for emerging technologies, such as enhanced geothermal systems, CO_2-enhanced shale oil recovery, and caprocks for geologic carbon storage, are typically characterized by low permeability and rely heavily on creating or restricting fluid transport through natural and induced fractures. However, our fundamental understanding of how fractures respond to reactive fluid injection under relevant subsurface conditions remains limited, particularly with respect to feedback among geochemical and geomechanical alterations (Detwiler, 2008; Yasuhara & Elsworth, 2008). Chemical reactions, namely dissolution of primary minerals and precipitation of secondary minerals from interactions between pore fluids and the host rock, can critically alter fracture permeability and mechanical stability (Detwiler, 2008). Intuitively, permeability increases under advection-dominated flow due to free surface mineral dissolution and reaction front instabilities (i.e. wormholing)(McGuire et al., 2013; Polak et al., 2004) and decreases when secondary precipitates fill pores and fractures, which typically requires longer fluid residence times with diffusion-dominated flow. However, dissolution and compaction of critical asperities (i.e. contact points between fracture surfaces) can lead to permeability reductions despite net dissolution and increased porosity,(Ellis et al., 2013; Walsh et al., 2013; Yasuhara & Elsworth, 2008) which precipitates could counteract by serving as proppants between fracture walls or by generating sufficient crystallization stress to induce tensile fracturing in the surrounding rock (Lisabeth et al., 2017; Noiriel et al., 2010). The mechanical implications of chemical alterations are further complicated by heterogeneities in composition and structure, as preferential dissolution of more reactive minerals creates porous non-reactive layers that inhibit further reactions along the fracture surface (Deng et al., 2018). Improved knowledge of which fracture alteration mechanisms will predominate in a reactive geological system is imperative to predicting permeability evolution at reservoir scales, but to date few experimental studies have explored the dynamics of competing geochemically mediated deformation processes.

While the impacts of mineral dissolution on fracture alteration and fluid transport have been well-documented,(Detwiler, 2008; Garing et al., 2015; Noiriel et al., 2013; Polak et al., 2004) precipitation remains relatively enigmatic due in part to inherent difficulties in creating favorable conditions in the lab. Even though the necessary thermodynamic and kinetic conditions are well understood, precipitates often fail to precipitate or otherwise form non-uniformly in relatively uniform environments due to complex interactions among contributing factors that are difficult to resolve or anticipate. For example, Emmanuel and Berkowitz demonstrated through numerical modeling that mixing-induced precipitation can clog some high-porosity regions while others remain unaltered despite conditions appearing equivalent (Emmanuel & Berkowitz, 2005). Precipitation is controlled by a range of chemical and structural factors including mineralogy; pore and grain size distributions; fluid chemistry; and reaction kinetics of the dissolving and precipitating phases. Dissolution-precipitation kinetics are particularly challenging to predict at local scales because rates depend strongly on specific surface area, which evolves nonlinearly with changing porosity(Emmanuel & Berkowitz, 2005) and remains poorly constrained in numerical modeling. Furthermore, heterogeneities in all of these parameters can promote strongly localized precipitation that might be overlooked in high-level reservoir simulations but can significantly alter bulk fluid transport if precipitates form along critical flow paths. For instance, during flow through a fractured cement core, Huerta et al. observed that heterogeneous aperture distributions led to fast non-uniform precipitation near the inlet and subsequent flow diversion and channelization (Huerta et al., 2013). Even spatially uniform precipitates can lead to non-uniform transport alterations as narrow fractures and pore throats may be preferentially sealed (Beckingham, 2017).

Precipitates reduce overall porosity but have diverse effects on permeability and pore size distributions. While precipitation generally favors smaller pores with higher reactive surface area, Emmanuel et al. found that precipitation was suppressed in pores less than 10 μm as interfacial energy effects led to increased solubility (Emmanuel et al., 2010). In basalt carbonation experiments, Luhmann et al. also observed preferential precipitation in larger pores while the volume of smaller pores and overall specific surface area increased due to dissolution (Luhmann et al., 2017). Even when changes in porosity are constrained, implications for permeability are complex. Noiriel et al. reported that permeability alterations resulting from calcite precipitation in porous columns containing mixtures of glass beads and crushed $CaCO_3$ depended strongly on changes in pore roughness in addition to pore volume; in two columns that experienced comparable decreases in overall porosity, one experienced a greater increase in pore roughness that led to more heterogeneous flow fields and greater reductions in permeability (Noiriel et al., 2016). The location of precipitates is also significant because pore networks tend to converge and diverge erratically such that even a slight change in overall porosity can substantially impact permeability (Pruess & Müller, 2009). For instance, an earlier study by Noiriel et al. reported that dissolution increased the permeability of a limestone core by an order of magnitude while porosity remained nearly constant (Noiriel, 2004). Porosity-permeability relationships in a given system cannot be effectively predicted with any single geochemical variable (Nogues et al., 2013) and are highly contingent on the spatial distribution of geochemical reactions, particularly when

precipitation is involved (Beckingham, 2017). In CO_2 percolation experiments on sintered olivine cores, Peuble et al. reported substantial permeability reductions despite relatively insignificant reductions in overall porosity, which they primarily attributed to localized precipitation that obstructed transport in primary flow paths (Peuble et al., 2015). Hysteresis effects also complicate modeling efforts, as dissolution-driven permeability increases have been shown to proceed much faster than precipitation-driven permeability reductions (Nogues et al., 2013). Overall, contradictions among previous results emphasize the challenges associated with accurately predicting how precipitation will affect long-term fracture permeability given the complexity and uncertainty of interactions between geochemical and geomechanical alterations.

In light of the relative dearth of research surrounding the timing, extent, and significance of mineral precipitation in subsurface systems, the objective of this work was to determine how geochemical reactions impact fracture permeability and microstructure with a targeted focus on the role of secondary precipitates. While most precipitation studies have concentrated on the mixing of incompatible fluids to force precipitation from supersaturated fluids,(Emmanuel & Berkowitz, 2005; Jones & Detwiler, 2016; Tartakovsky et al., 2008; Zhang et al., 2010) we explicitly focused on reactions between the injected fluid and host rock. Following preliminary testing to evaluate the reactivity of different rock and fluid compositions, a series of triaxial direct shear experiments was conducted on carbonate-rich shales using $BaCl_2$-rich solutions as the working fluid. Experiments were carried out within an x-ray computed tomography (xCT) scanner, allowing for non-destructive 4D imaging of *in situ* reactions under representative subsurface stress conditions (Carey, et al., 2015). Computed tomography has been applied extensively in studies of flow through porous media, most frequently under ambient unstressed conditions due to inherent challenges in designing and building experimental systems with x-ray compatibility (Wildenschild & Sheppard, 2013). Frash et al. (2016) were the first to combine *in situ* xCT with direct shear fracturing and permeability measurements under high confining stress, which allows for direct characterization of stress-dependent fractures and avoids damage during stress cycling. Here, the experimental system was designed to create favorable geochemical conditions for mineral precipitation and to optimize the likelihood of observing precipitate evolution in real time. Disequilibrium in pore fluids following $BaCl_2$ injection drives calcite ($CaCO_3$) dissolution in the host rock, releasing carbonate ions to solution that can then combine with Ba^{2+} to form barium carbonates ($BaCO_3$) when critical saturation levels are achieved and nucleation becomes favorable. The fast dissolution and precipitation rates of $CaCO_3$ and $BaCO_3$, respectively, were expected to promote these reactions over experimentally relevant time scales. Note that barium carbonates are rare in natural systems but were selected here to provide effective x-ray contrast between the host rock and secondary mineral phase, as $BaCO_3$ is roughly 1.6 times denser than $CaCO_3$ and has exhibited strong xCT visibility in prior work (Carey et al., 2016). The conversion of $CaCO_3$ to $BaCO_3$ also involves a 27% increase in solid volume, which could compete with dissolution or compaction mechanisms for control on overall permeability.

2. Experimental design and data analysis

This section presents precursory results motivating the design of the three experiments presented here as well as general methodology and details on the system setup for all shear tests. Section 2.1 summarizes key results from preliminary batch experiments that informed our selections of core samples and injected fluid chemistry, which are detailed in Section 2.2. Section 2.3 provides an overview of the triaxial system setup, including sample assembly, data collection, and x-ray imaging. Further details on x-ray radiography and scan optimization along with techniques for xCT data processing and post-reaction sample characterization are provided in Section 2.4.

2.1. Preliminary reactivity testing

Initial batch experiments were conducted to determine the relative reactivity of various carbonate-rich materials. Marble and limestone cores (>99% calcite) were obtained from Kocurek Industries and carbonate-rich shales were provided by Chesapeake Energy Corporation and the National Energy Technology Laboratory. Chips saw-cut from cores of each rock were reacted in solutions of 20, 2,000, and 180,000 ppm $BaCl_2$ for 12 hours under ambient conditions. One half of each chip surface was lightly roughened prior to reaction to simultaneously evaluate the potential impact of freshly activated surfaces. The reacted chips were characterized via scanning electron microscopy (SEM) with back-scattered electron imaging (BSE) and energy-dispersive x-ray spectroscopy (EDS). Minimal reaction products were observed at 20 ppm $BaCl_2$ but barium carbonates formed at 2,000 and 180,000 ppm, with the extent of precipitation greatest at 180,000 ppm. Precipitate morphologies varied from fine needles to more prismatic crystals depending on the substrate material (Figure 1) and generally aggregated in larger masses that often coated $CaCO_3$ surfaces in the shale and marble chips, but most limestone samples contained only a few isolated $BaCO_3$ crystals (not shown) or sparse clusters of finer precipitates (Figure 1d). Reasons for this discrepancy are unclear considering that the marble and limestone samples were compositionally equivalent and limestone should theoretically dissolve more readily because the porosity and permeability are greater. In general, precipitates also exhibited a preference for freshly roughened over weathered surfaces, suggesting that freshly sheared fractures with abundant reactive surface area would be more conducive to precipitation than saw-cut or pre-fractured samples. This observation motivated the application of triaxial shear tests in this work as opposed to traditional flow-through experiments examining dissolution-precipitation reactions in whole or pre-cut cores.

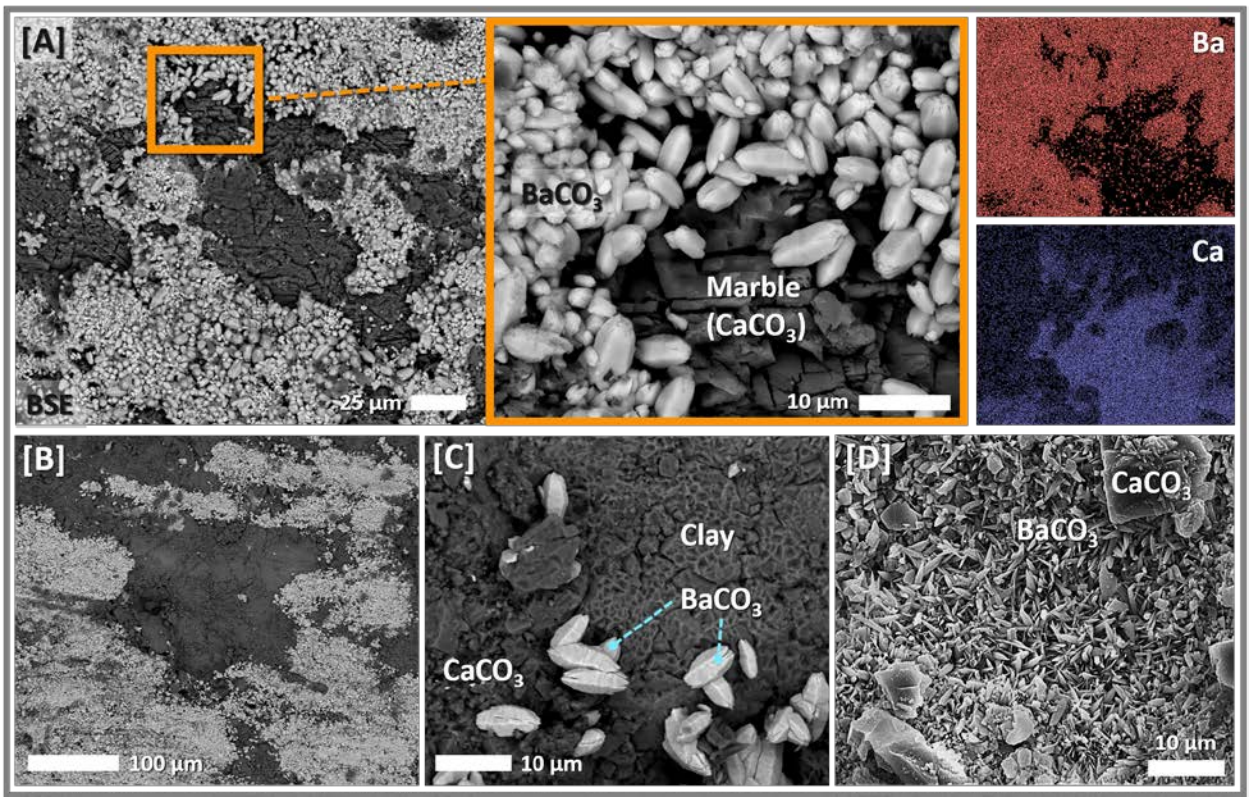

Figure 1. Example BSE images and EDS maps revealing small $BaCO_3$ crystals on the surfaces of [A] marble, [B,C] calcite-rich shale, and [D] limestone reacted in solutions of 2,000 ppm $BaCl_2$ at ambient conditions.

2.2. Geochemical conditions: Shale cores and fluid chemistry

An initial experiment, reported by Carey et al.(Carey et al., 2016) and described in Section 3.1, resulted in extensive $BaCO_3$ precipitation during shearing of a carbonate-rich Utica shale that was inadvertently exposed to $BaCl_2$-rich fluid. This core, provided by Chesapeake Energy Corporation, was taken from a depth of 1817 m (5960 ft) and consisted of 93% calcite, 2% dolomite, and 5% quartz according to compositional data provided by the company. Juxtaposing the results from this test with the limited extent of precipitation observed in preliminary batch testing with nearly pure calcite rocks (marble, limestone), it was hypothesized that the extensive microfractures formed during shale fracturing uniquely supported the development of secondary minerals. Thus, two shale samples with relatively high calcite content were selected to build on the initial Utica experiment. A similar Utica core plug (also provided by Chesapeake Energy Corporation) was taken from a depth of 1813 m (5948 ft) and contained 82% calcite, 4% quartz, and 10% clay with 1% each of dolomite, organic carbon, pyrite, and apatite. A second core was obtained from a Marcellus shale outcrop and was comprised of 66% carbonate, 19.5% quartz and feldspar, 13% clay, and

1.7% accessory minerals. Core plugs were trimmed to 25.4 mm (1") in length and measured approximately 25 mm in diameter. While conventional triaxial experiments use a 2:1 length:diameter ratio, a 1:1 ratio was applied here to promote fracturing throughout the entire length of the samples for practical permeability measurements.(Frash et al., 2016)

As described in Section 2.1, initial batch experiments on shale and calcite samples revealed $BaCO_3$ formed in 2,000 and 180,000 ppm $BaCl_2$ solutions but was negligible at 20 ppm. The highest tested concentration (180,000 ppm) was ultimately selected as the primary working fluid for shear fracturing in this study to induce visible precipitation within hours of commencing fluid injection such that precipitate evolution could be captured in xCT scans. Lower concentrations (200 or 2,000 ppm) were also applied as needed to improve x-ray contrast or to test the influence of pore fluid saturation on precipitation rates. Changes in fluid chemistry for each test along with the carbonate content of the cores are summarized in Table 1 and detailed in Section 3.

2.3. Triaxial direct shear with x-ray imaging

Figure 2 illustrates the sample assembly for direct shear testing. Cores were first positioned between two asymmetric semi-circular stainless-steel thrust collars that focus shear stress along a central plane, with porous screens placed between each collar and core end. Channels built into the collars allow for fluid flow into and out of the core. All samples were aligned with the shear platens oriented 45° to bedding planes because previous work has indicated that the resulting fracture permeability peaks when shearing occurs near this angle (Carey et al., 2015). As noted previously, these experiments were designed to maximize the potential for observing reaction-induced fracture alterations in real time, so this fracture alignment was selected to maximize the probability of generating fracture apertures that were large enough to be observed in x-ray radiography under elevated stress conditions. This setup is also relevant to field applications as bedding planes are ubiquitous in natural systems and are often subjected to shear stresses at varying orientations in oil and gas shales (Weng et al., 2018).

Because nitrogen gas was used as the confining fluid to optimize x-ray transparency, a rubber sleeve (EPDM) was placed around the core and collars to prevent N_2 intrusion. The assembly was jacketed with chemical-resistant heat-shrink tubing (FEP), secured with wire tourniquets on the upper and lower collars for reinforced sealing, before being loaded into a triaxial core holder comprised of aluminum for x-ray transparency. The core holder and all upstream and downstream flow lines are built into a Hytec cabinet equipped with a 150 kV Hamamatsu micro-focus x-ray tube and Varian panel with 127-μm pixels for live x-ray imaging and micro-computed tomography. Additional details on the system's design and capabilities are provided by Carey et al.(Carey et al., 2015) and Frash et al.(Frash et al., 2016, 2019)

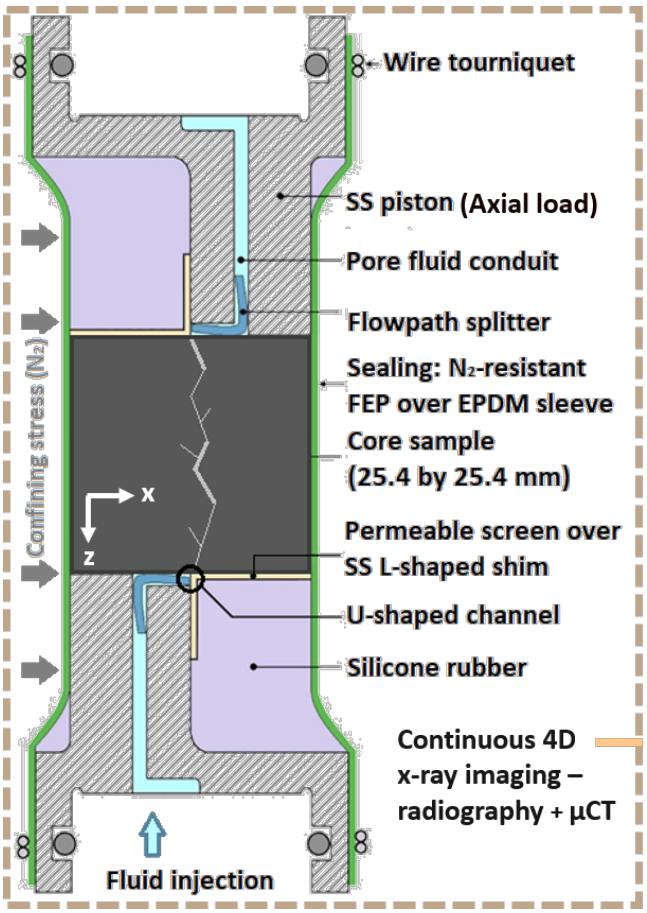

Figure 2. Schematic of triaxial direct shear system sample assembly, adapted from Frash et al.(Frash et al., 2019) The sample assembly is loaded into an aluminum triaxial core holder within a µCT scanner. The reference axes used in xCT analyses are shown relative to the core orientation, with the y-axis perpendicular to the x-z plane in the figure.

Three triaxial direct shear experiments were conducted to promote mineral precipitation during shear fracturing, as summarized in Table 1 and described in detail in the results. Each experiment involved one or more shear events with varying concentrations of $BaCl_2$ in the pore fluid to test the influence of fracture geometry and fluid chemistry, respectively, on secondary precipitation and resulting impacts to fracture permeability and structure. We also selected cores with varying calcite fractions to test the hypothesis that the extent of precipitation would increase with increasing reactive mineral content. All experiments were conducted at room temperature (~20°C) under varying stress conditions that are detailed for each experiment below. Fluids were injected with high-pressure syringe pumps (Teledyne ISCO) controlled by DIsco software,(Frash, 2016) which also records flow, pressure, and displacement data. The upstream and downstream pore pressures were held at 1.5 and 0.5 MPa, respectively, and confining stress was held at 3.5 MPa

for initial shear events. Cores were directly sheared by increasing the axial stress with a constant flow rate of 0.5 mL/min through the axial pump until failure occurred, after which the system was allowed to stabilize at isotropic stress conditions. Permeability was measured continuously based on flow rate and pressure readings recorded by the pumps and high-precision Quartzdyne pressure transducers installed upstream and downstream of the core. Displacement was monitored with a linear variable differential transformer (LVDT) mounted on the upper (downstream) end of the triaxial cell. X-ray radiographs were also taken continuously at a rate of 3.75 frames per second while xCT scans were taken at points of critical changes in experimental conditions.

Table 1. Summary of key experimental conditions

Condition	US-01	US-02	MS-01
Shale formation	Utica	Utica	Marcellus
Carbonate content	93%	82%	66%
Confining stress*	3.5 MPa	3.5 MPa	3.5 MPa
Upstream pore P	1.5 MPa	1.5 MPa	1.5 MPa
Downstream pore P	0.5 MPa	0.5 MPa	0.5 MPa
Shear orientation	45° to bedding	45° to bedding	45° to bedding
Injected [$BaCl_2$]	Not measured**	180,000 ppm	200 → 2,000 → 180,000 ppm
Injectate pH+	--	6.9	7.1 → 7.1 → 6.9
xCT scan timings	End of experiment	After each confining step	After adjusting [$BaCl_2$]

*Confining stress during initial shearing; note that confining stresses were subsequently changed to evaluate stress-permeability relationships as detailed in the text.

**In this experiment, DI water was used as the injected fluid and the [Ba^{2+}] was not directly measured because it was residual from a previous test using 18 wt% (180,000 ppm) $BaCl_2$ as a contrast agent (Carey et al., 2016).

+Initial pH of injected $BaCl_2$ solution calculated in CrunchTope(Steefel et al., 2015) with equilibrium constants from the EQ3/EQ6 thermodynamic database. Note that pH values are approximate as they are based on activity coefficients calculated using the extended Debye-Huckel equation with the B-dot extension that are not accurate for high ionic strength solutions.

2.4. Post-reaction xCT analysis and sample characterization

In the initial experiment (US-01), x-ray radiography was collected continuously at a rate of 0.7 frames per second but only one *in situ* xCT scan was acquired at the end of the test. All x-ray data were collected in the industrial µCT scanner described in Section 2.3 at a beam energy of 150 kV with a 25-µm spot size. For the next two experiments, xCT scan parameters were optimized for

speed and quality in order to capture rapid changes in mineralogy and fracture structure. Preliminary testing revealed high-power scans (150 kV, 500 μA) lasting approximately 17 minutes provided sufficient quality for processing and segmentation within a reasonable time frame. Scans were taken at a rate of 3.75 fps with 800 projections and 5-frame averaging. Voxel resolutions were approximately 27 μm in US-01 and 46.5 μm in US-02 and MS-01.

Raw radiographs were calibrated with light corrections taken in the empty chamber and dark corrections collected with the x-rays off. All xCT scans were reconstructed using RECON software at LANL. Ring removal was applied to reduce noise in the images, which were output as TIF stacks for further processing. Fractures were first segmented in MATLAB (version 2016b) using a simple thresholding process to create a binary 3D dataset where the z axis is parallel to the direction of shear along the length of the core; x is perpendicular to the shear direction; and y is perpendicular to the shear (xz) plane (Figure 2). Aperture maps were then generated by summing the fracture voxels in each column (y axis on 2D cross sections) along the x axis over the length of the core (z axis). Note that black (zero-aperture) regions are not necessarily completely closed but are below the voxel resolutions of the xCT scans (27 μm in US-01; 46.5 μm in US-02 and MS-01). Excluding scan artifacts due to rings and beam hardening, the uncertainty in segmentation calculations is within ±1.5 voxels (i.e., 40.5 μm for US-01 and 70 μm for US-02 and MS-01). Because both samples contained Fe-bearing accessory minerals (mainly pyrite) exhibiting a similar x-ray intensity as $BaCO_3$, the precipitates were segmented in sections along the direction of shearing that excluded high-intensity primary minerals from the analysis. Precipitation maps were created with the same workflow as the aperture maps to facilitate comparison between the spatial distributions of precipitates and fractures. Areas with no resolvable precipitate volumes may still contain small crystals or surface coatings of secondary minerals, but due to the complex factors controlling CT intensity in voxels with multiple potential components (e.g. shale, voids, precipitates, pyrite, etc.), we did not estimate the volume of precipitate that that could be missed by our segmentation method. In US-02, segmented fracture and precipitate volumes were also summed across the core for each scan to quantify changes with increasing confining stress (section 4.4). Note that scans taken during injection of 180,000 ppm $BaCl_2$ were not segmented due to limited contrast between the injected fluid within fractures and surrounding shale.

After non-destructive analyses were complete, fractured samples were secured in heat shrink tubing and vacuum-impregnated with epoxy for sectioning. Thin sections oriented 45° to the primary shear fractures were characterized via SEM with BSE imaging, using EDS mapping and point analyses to obtain compositional data on reaction products. Note that while EDS provides chemical data on mineral phases from which compositions can be inferred, it is not a tool for explicit mineral identification. More refined techniques to determine exact crystal structures and zoning were not pursued because the focus of this work was on factors driving precipitation, where the extent of precipitates was more important than their composition, and precipitate volumes were too small for destructive analyses such as x-ray diffraction.

3. Triaxial direct shear fracturing

The following sections present methodology and results for each experiment. Section 3.1 details experimental procedures for each test with corresponding lab data (i.e. shear stress, confining stress, permeability, and injectate [$BaCl_2$]) and provides context for changes in stress and fluid conditions within and among experiments. Sections 3.2. 3.3, and 3.4 then provide results from xCT analyses and post-reaction sample characterization for US-01, US-02, and MS-01, respectively. Stress-permeability data are also included in these sections to highlight where changes in stress-permeability data correspond to precipitation and fracture alterations observed in x-ray imaging. Refer to Table 1 for details on experimental conditions.

3.1. Series overview: Experiment procedures and stress-permeability data

Figure 3 compares stress-permeability data for each experiment. Changes in confining and direct shear stress are plotted on the left axes; resulting changes in permeability based on recorded pressure differentials and flow rates are plotted on the right axes; and changes in injected (pore) fluid chemistry during US-02 and MS-01 are denoted by the shaded regions with labeled [$BaCl_2$]. Note that these data are also included in the individual results sections for each experiment to mark points where xCT scans and select radiographs were taken.

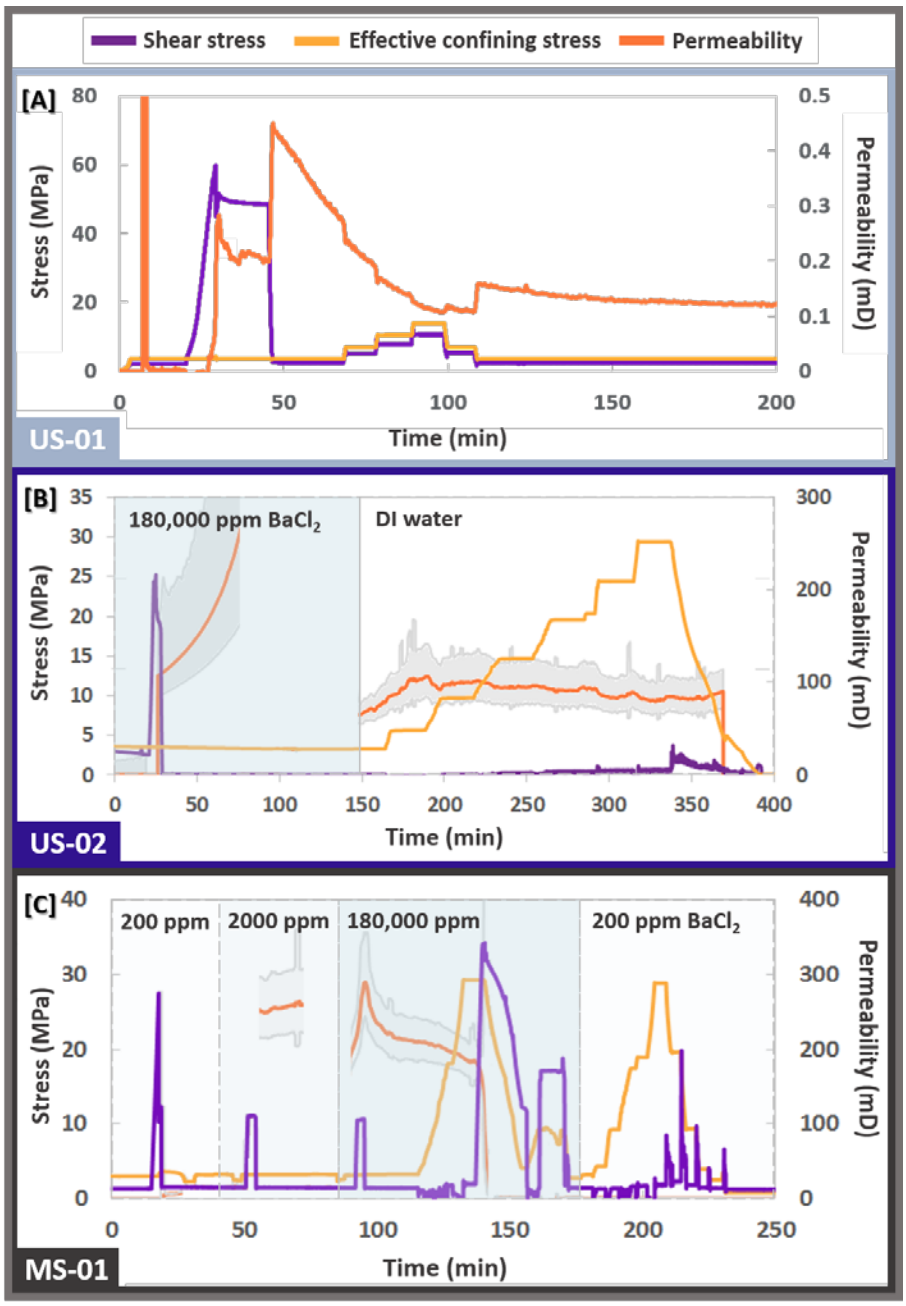

Figure 3. Stress-permeability data for the series of three triaxial direct shear tests, highlighting experimental procedures with respect to changes in stress and fluid conditions in [A] US-01, [B] US-02, and [C] MS-01. Shear and confining stress are displayed on the left axis, permeability is presented on the right, and changes in injected fluid chemistry are denoted by the labeled shaded regions for US-02 and MS-01. Note that for US-01, DI water was injected throughout the test but the core was exposed to up to 180,000 ppm of residual $BaCl_2$ in the pore lines. Experimental conditions are summarized in Table 1.

The first experiment (US-01) involved direct shearing of a nearly pure-carbonate Utica shale core that was used as received (i.e., partially dehydrated). The intended pore (i.e. injection) fluid was DI water but the core was initially subjected to a $BaCl_2$-rich solution that had not been completely purged from the pore lines following a prior test. Carey et al. estimated this solution was dilute, containing ~19.5 ppm Ba^{2+}, but results from the subsequent experiments conducted here indicate the actual concentration was at or near the 180,000 ppm that had been used in the prior test (Carey et al., 2016). The core was initially sheared under 3.5 MPa confining stress, where shear failure was marked by a sharp drop in direct shear stress around 80 MPa and concomitant increase in permeability from <1 μD to ~0.25 mD (Figure 3a). Axial stress was held above 60 MPa for the next 15 minutes, during which time permeability gradually decreased to ~0.2 mD, and then the stress was returned to isotropic conditions (3.5 MPa) while permeability rose sharply again to a peak of 0.43 mD. Confining stress was incrementally raised to 7, 10.5, and 14 MPa for stress-permeability measurements that are not discussed in this study and then decreased in the same steps to return to 3.5 MPa. Each change in confining stress produced a sharp drop in permeability followed by a continuing steady decrease until the next stress step. Continuous x-ray radiography provided live imaging of the primary fracture and a post-reaction xCT scan was taken *ex situ* (i.e., without confining stress) to obtain 3D imaging. Radiographs evidenced opaque precipitates forming within 10 minutes of shearing that motivated the subsequent experiments, as detailed in Section 3.2.

In the second test (US-02), a less calcite-rich Utica core was used as received (i.e., partially dehydrated) with an initial condition of 180,000 ppm $BaCl_2$ injection fluid at the upstream face of the core. As noted in the methods, this concentration was selected because (a) it was the maximum value the core in US-01 would have been exposed to and (b) preliminary testing revealed barium carbonates formed quickly on calcite-rich samples reacted in 180,000 ppm $BaCl_2$ solutions (Section 2.1). The upstream pore pressure was held constant at 1.5 MPa and back pressure at 0.5 MPa using syringe pumps with a maximum flow limit set at 0.25 mL/min. A pre-reaction xCT scan was taken under 3.5 MPa isotropic stress before the core was sheared to 1 mm displacement at 3.5 MPa confining pressure. The axial stress was then increased until the sample failed around 25 MPa (Figure 3b). Upon shear failure, the permeability rose sharply to ~100 mD and then continued to increase to a maximum of ~235 mD before falling to ~50 mD while the flow lines were purged with DI water to improve x-ray contrast. Back-to-back xCT scans were taken immediately after shearing to capture mineral dissolution-precipitation reactions resulting from continuous flow of the high-[$BaCl_2$] fluid through fresh fracture networks. Because the high [Ba] impeded x-ray contrast between the fracture and surrounding rock, the injection fluid was replaced with DI water after the second scan. Following fluid breakthrough, evidenced by lightening of the fracture as DI replaced the dense $BaCl_2$ solution, another xCT scan was taken before raising the confining pressure in successive steps (6, 10, 15, 20, 25, and 30 MPa) to obtain fracture aperture and permeability data under varying effective stress states. An xCT scan was taken at each step to characterize fracture evolution with increasing stress and to capture potential dissolution-precipitation reactions in real

time. Radiography was recorded continuously between all xCT scans with the x-ray beam aligned parallel to the opposing direct shear platens and resulting fractures.

The final experiment (MS-01) involved more shear steps and fluid changes. After a pre-reaction xCT scan, the Marcellus core was sheared to 0.5 mm of displacement under 3.5 MPa confining stress with a lower concentration of 200 ppm $BaCl_2$ in the pore fluid to evaluate precipitation potential at low $BaCO_3$ supersaturation. Upstream and downstream pressure limits were maintained at 1.5 and 0.5 MPa, respectively, with a flow limit of 1 mL/min. Another xCT scan was taken immediately after shearing and the pore fluid was then replaced with a 2,000 ppm $BaCl_2$ solution to enhance the likelihood of precipitation, as no precipitates were observed in the live radiographs during the initial shear event and subsequent stabilization. The more concentrated 2,000 ppm solution was injected at a higher flow rate (10 mL/min) until it reached the core, at which point the original flow limits were restored and the sample was re-sheared to 1 mm displacement while maintaining 3.5 MPa confining stress. After collecting a post-shear xCT scan, the pore fluid was replaced with 180,000 ppm $BaCl_2$ to improve the likelihood of precipitation and the process of re-shearing (to 1.5 mm displacement) and xCT scanning was repeated. Similar to US-02, fluid breakthrough was determined by a change in contrast in x-ray radiographs, where increasing [$BaCl_2$] increased the opacity in the shear fracture. Note that the first peak in the shear stress curve (Figure 3c) represents the stress required to induce shear fracturing in the original specimen, while subsequent peaks correspond to the residual stress required to re-activate this fracture. Following the third shear step and xCT scan, the confining stress was raised to 30 MPa and the core was re-sheared. Axial stress was then held constant and the core was dynamically sheared by steadily releasing confining stress to 5 MPa, which induces additional shear displacement as falling confining pressure causes the pistons to slide. The aim of this process was to promote further fracturing in the core and test the hypothesis that because this core had the lowest calcite content, more freshly activated fracture surfaces needed to be created to expose sufficient calcite-rich regions for observable dissolution and precipitation to occur.

The remaining shear displacement steps in this experiment were imposed to study stress-permeability relations that are not the primary focus of this work, but are included in this study because they affected the final state of the core with respect to fracture geometry and secondary precipitation. Once the system had stabilized after dynamic shearing, the core was hydrosheared by raising the pore pressure to 2 MPa under a constant 10 MPa confining stress. Hydroshear refers to shear induced by fluid flow through a fracture as opposed to shear induced by the external shear stress created by increasing the axial piston displacement in previous steps. This step was conducted here to demonstrate whether effective stress conditions leading to hydroshear were equivalent to those for external shear for the Marcellus core, which was not a primary objective of this study. Following this step, the pore fluid was replaced with 200 ppm $BaCl_2$ to improve x-ray contrast, and confining stress was incrementally raised to 3.5, 5, 10, 20, and 30 MPa to obtain stress-aperture data. The confining stress was then lowered in the same increments with additional measurements taken at each step. Each step down in confining pressure induced a shear event,

evidenced by the sharp peaks in direct shear stress toward the end of the test (Figure 8a). A final xCT scan was taken before depressurizing the system and removing the core, which was secured in heat shrink tubing to prevent loss of precipitates and fragments generated in shearing.

3.2. US-01: High-carbonate Utica shale

Results from the first shear experiment are summarized in Figure 4. After peaking at 0.43 mD, the permeability fell steadily over the remainder of the experiment, which included a series of step increases in confining stress to obtain stress-permeability data that is not the focus of this study. During this time, continuous x-ray radiographs evidenced opaque white material accumulating in the fracture (Figure 4b). The permeability increased slightly as confining stress was returned to 3.5 MPa in the final stage of the experiment and then decreased gradually over the next 5 hours as the system was held under isotropic stress conditions, reaching a final value of 0.084 mD that reflects an irreversible loss of permeability compared with the permeability measured directly following fracturing.

A post-reaction xCT scan revealed the opaque materials observed in radiographs corresponded to dense precipitates that ultimately filled much of the fracture network. Cross sections taken parallel (Figure 4d) and perpendicular (Figure 4e) to the direction of shear indicated precipitates were concentrated at the inlet and outlet of the core, which is demonstrated in the map of segmented precipitates (Figure 4c) that shows their spatial distribution in a 2D projection perpendicular to the shear plane. Fracture apertures were also segmented but note that because most of the original fractures were filled with precipitate, this map does not represent the original post-shear fracture network.

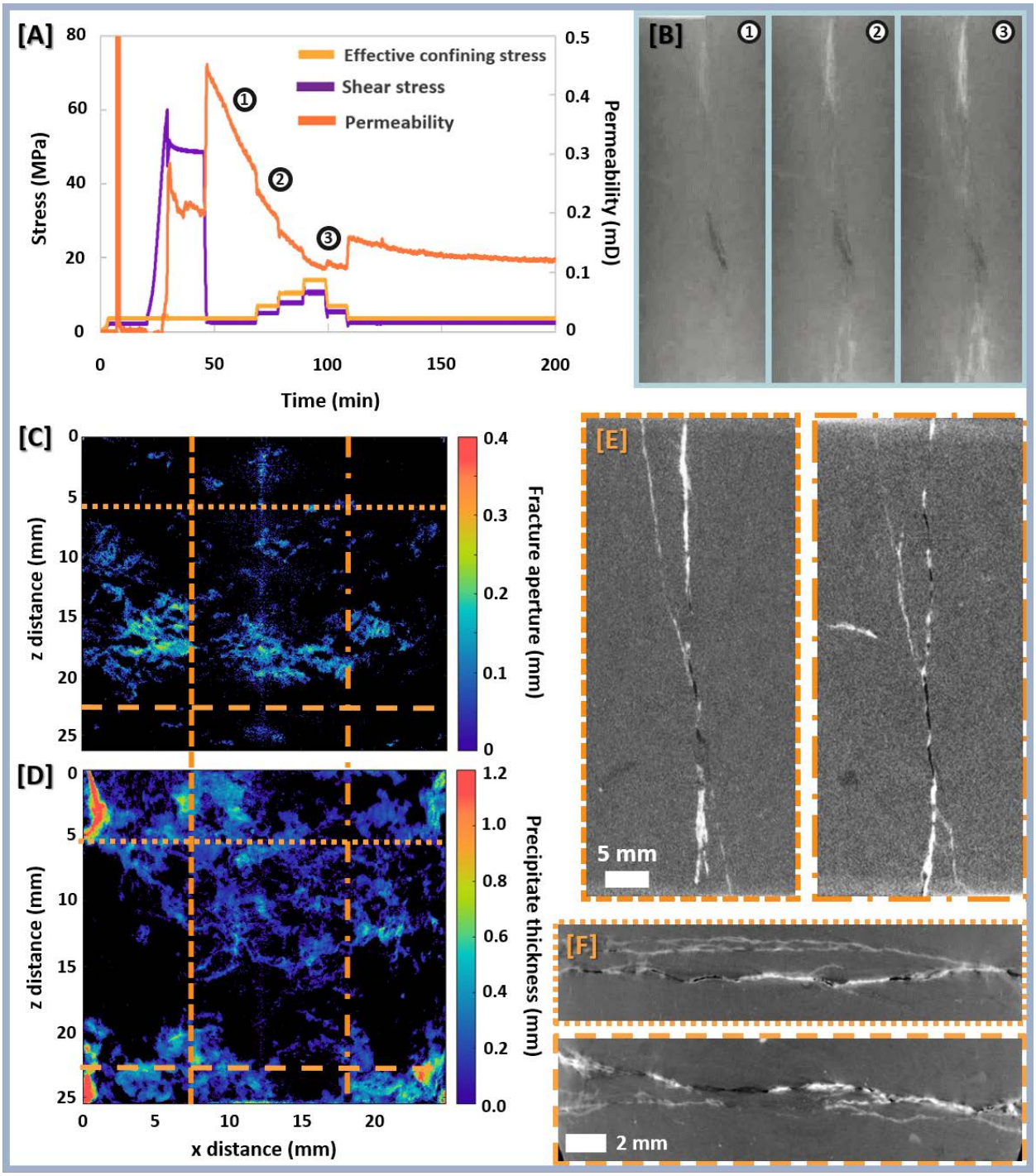

Figure 4. Summary of stress-permeability, x-ray radiography, and processed xCT data for US-01. [A] Changes in axial and confining stress, permeability, and pore pressure during the experiment. [B]

Radiographs at the time points marked in [A] showing opaque white precipitates accumulating at the inlet and outlet of the main fracture, concomitant with declining permeability. A post-reaction xCT scan was segmented illustrate spatial distributions of [C] fracture apertures and [D] precipitates, both shown in 2D projections perpendicular to the shear plane. Dashed, dash-dot, and dotted lines delineate positions of cross-sections highlighted in E and F that reveal white precipitate infill. The sections in [E] were taken perpendicular to the primary shear fracture along the length of the core (y-z plane) and those in [F] were taken in the x-y plane along the direction of shear.

Precipitates were identified as barium carbonates in SEM analysis of a thin section cut 45° to the primary shear fracture. Select BSE images and EDS maps indicating the presence of $BaCO_3$ within the $CaCO_3$-rich shale matrix are presented in Figure 5. Some fracture networks were essentially cemented with precipitates, which generally formed as needle-like crystals perpendicular to fracture walls. The SEM observations revealed greater concentrations of precipitates in regions with smaller apertures and with significant fragmentation or fault gouge (Figure 5).

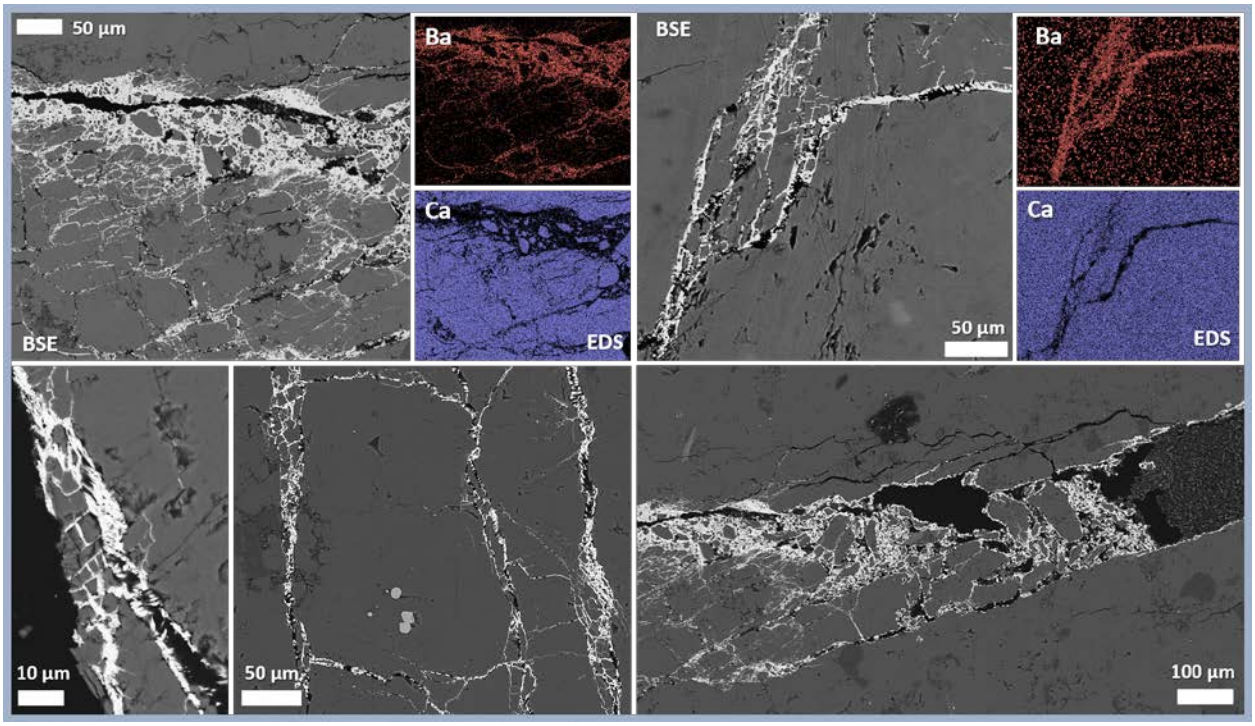

Figure 5. Example BSE images and select corresponding EDS maps from a thin section cut 45° to the primary shear fracture in US-01. EDS revealed $BaCO_3$ precipitates within fractures in a $CaCO_3$-rich matrix.

3.3. US-02: Carbonate-rich Utica shale

Stress-permeability and xCT data for the second Utica experiment are presented in Figure 6. Whereas only a post-reaction xCT scan was collected in US-01, a total of 10 rapid scans were taken over the course of this experiment to improve the temporal resolution of precipitation reactions. Successive xCT scans taken directly following shearing (locations 2 and 3 in Figure 6a) revealed that opaque white material, similar to precipitates observed in US-01, formed within 20 minutes of shearing. These precipitates were more clearly visible in a fourth scan collected after breakthrough of DI water. Following this scan, the confining pressure was increased incrementally to 30 MPa with an xCT scan taken upon stabilization at each step (5-10 in Figure 6a). Permeability increased to 112 mD as confining pressure was raised to 6 MPa and then decreased gradually to ~80 mD over subsequent step increases in confining stress (up to 30 MPa) due to fracture closures, as evidenced by aperture reductions across the 2D projections of fractures segmented from xCT scans in Figure 6d. Precipitates were also segmented (Figure 6c) but did not change significantly over the course of the experiment; their stability despite fracture closure is also apparent in the xCT cross sections (Figure 6b).

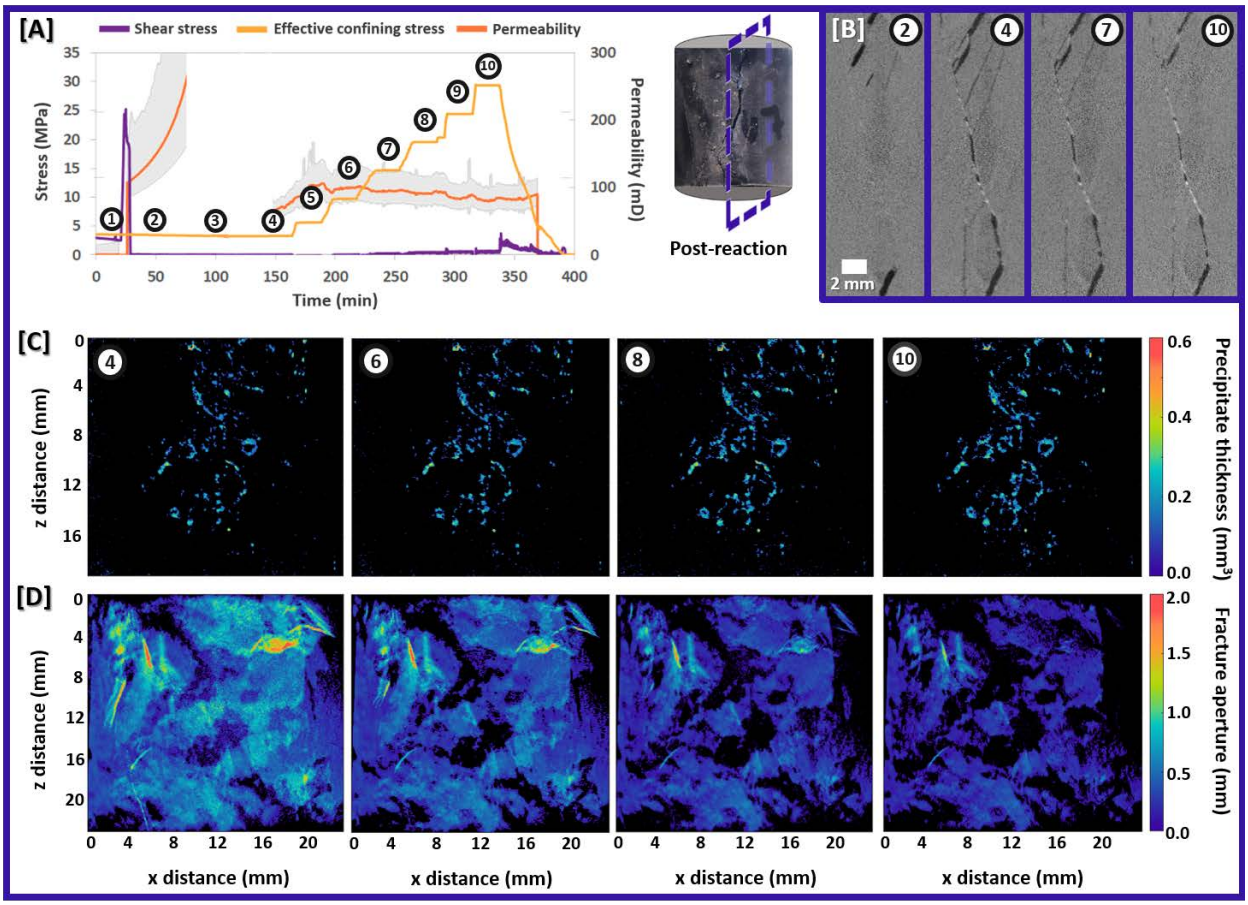

Figure 6. Summary of stress-permeability and xCT processing results for US-02. [A] Permeability evolution with changes in direct shear and confining stress, where grey shading corresponds to uncertainty in permeability measurements and blank regions indicate data were invalid. Circled numbers indicate where xCT scans were taken. The image of the core shows the location of the cross-sections in B-D. [B] Sections of selected reconstructed xCT scans along the primary shear fracture evidence precipitates forming within the first post-shear xCT scan and filling portions of the fracture. The xCT data were then segmented to map spatial distributions of [C] precipitates and [D] fracture apertures in 2D projections.

The reacted core was thin-sectioned 45° to the primary shear fracture for SEM analysis. Select BSE images and a representative combined EDS map identifying barium- and calcium-carbonates are presented in Figure 7. Precipitates did not cement fracture networks to the extent observed in US-01 but coated or filled fractures in many locations, particularly where apertures were narrow or fragmentation was abundant.

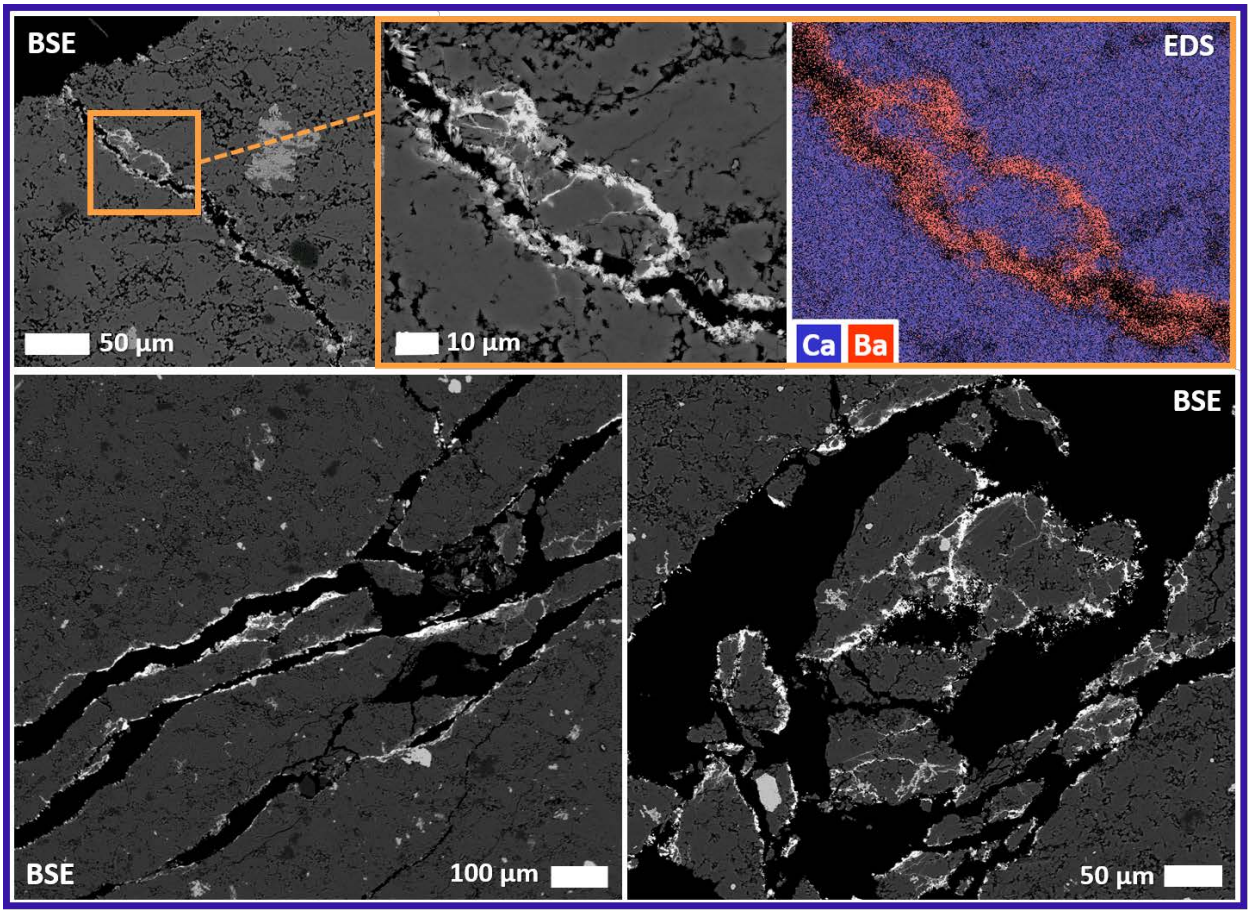

Figure 7. Example BSE and EDS images from a thin section cut 45° to the main shear fracture in US-02 highlighting $BaCO_3$ precipitation in microfractures.

3.4. MS-01: Carbonate-rich Marcellus shale

As detailed in Section 3.1, the final experiment on a carbonate-rich (66% calcite) Marcellus core was the most complicated with a series of three direct shear steps followed by dynamic shearing and hydroshearing. In Figure 8a, sample displacement aligning with each shear event is included below the stress-permeability data that was presented in Figure 1c. The core was displaced to 0.5 mm during the first shear event, 1.0 mm during the second, 1.5 mm during the third, and 3.2 mm during dynamic shearing. The series of ascending and descending confining pressure changes following hydroshear indirectly caused shear stress that resulted in slight further displacement to 3.4 mm. By contrast, the Utica cores were only displaced to a total of 0.9 and 1 mm in US-01 and US-02, respectively. Permeability rose to ~240 mD following the second shear event and ~280 mD following the third, after which it steadily decreased to 138 mD before suddenly plunging below 1 μD during dynamic shearing. Reasons for this permeability drop are discussed in Section 4.3.

An xCT scan was collected after each direct shear step (locations 1-3 in Figure 8a) and at the end of the experiment (4). Cross-sections from each scan are compared in Figure 8d, revealing that significant shearing occurred and white precipitates formed between the third direct shear step and the final scan taken ~2.5 hours later. The exact timing of precipitation is discussed in Section 4.1. Segmentation of the final xCT scan demonstrated that precipitation was concentrated at the inlet (Figure 8b) and in regions with small fracture apertures (Figure 8c). These observations are better visualized in xCT sections perpendicular to the direction of shear that depict precipitation favoring narrow gaps between fracture walls (Figure 8e). Comparing segmented 2D maps with xCT cross sections provides a more complete picture of *in situ* processes; for example, the region of greatest precipitation in the lower righthand corner of Figure 8b occurs in a region of small sub-resolution apertures (Figure 8c) that appear in the corresponding perpendicular xCT section (far right panel of Figure 8e) illustrating precipitation filling a narrow fracture at the core inlet.

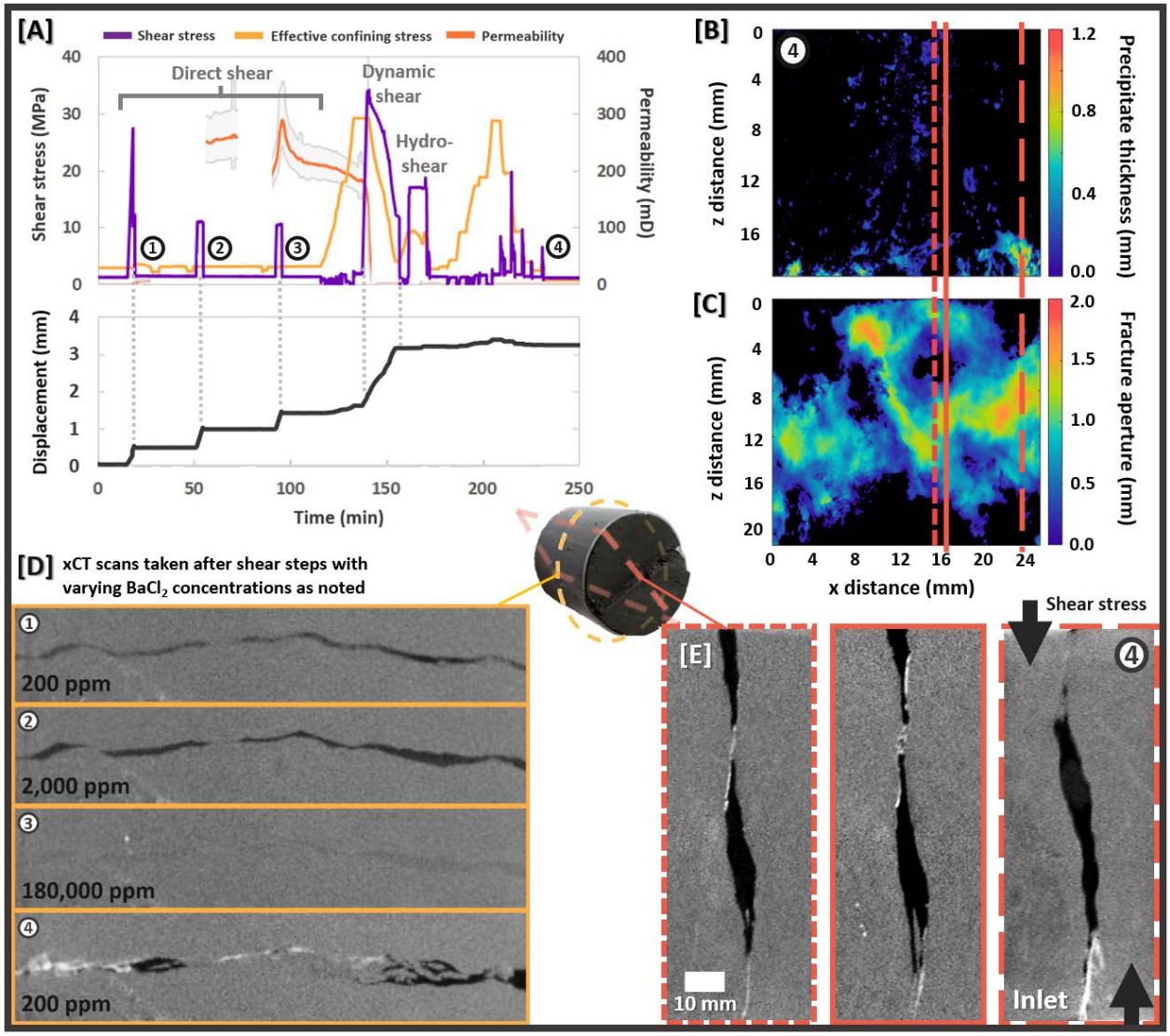

Figure 8. Summary of stress-permeability and xCT results for MS-01. [A] Permeability evolution with changes in direct shear and confining stress, where grey shading corresponds to uncertainty in permeability measurements and blank regions indicate data were invalid. Circled numbers indicate when xCT scans were taken. [B] Precipitate and [C] fracture aperture maps derived from segmentation of the final xCT scan (#4). Solid, dashed, and dotted lines show position of cross-sections in E. [D] Cross sections from post-shear xCT scans taken at the four locations noted in (A) that exemplify fracture and precipitate evolution with changes in stress and injected fluid chemistry. The location of cross-sections is shown in the central 3D image. [E] Sections from the final xCT scan taken perpendicular to the direction of shear, which represent y-z planes from the sections delineated in the x-z maps in [C] and [D]. White precipitates are evident in narrow regions between fracture walls.

Select BSE images from thin section analysis are provided in Figure 9 along with a representative EDS spectrum indicating that precipitates were barium carbonates. Consistent with observations in the xCT scans, precipitation was less abundant relative to the Utica experiments but more fault gouge formed due to the greater number of shear fracturing events and sample displacement.

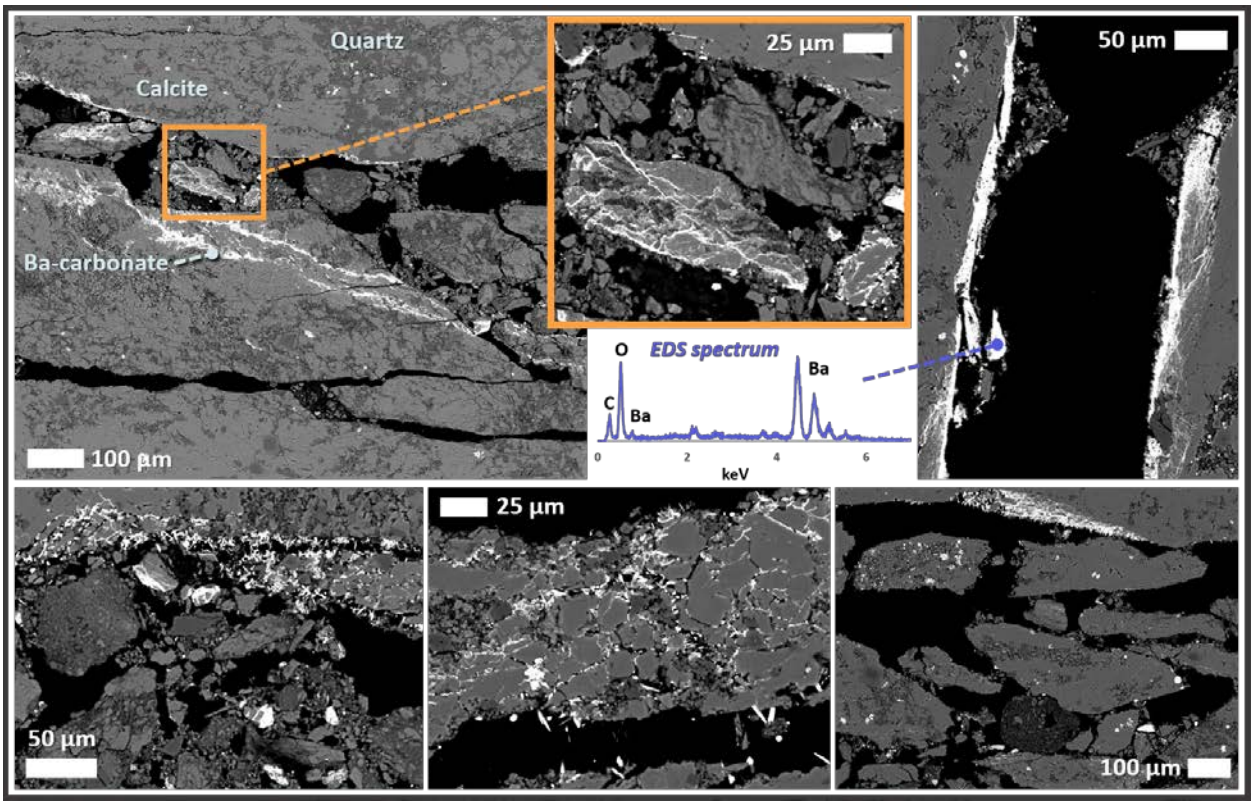

Figure 9. Select BSE images from a thin section cut 45° to the main shear fracture in MS-01. An example EDS spectrum for barium carbonate precipitate is included in the center.

Discussion

4.1. Rapid mineral precipitation

Within 10 minutes of shearing the original Utica shale (US-01), opaque secondary minerals appeared in x-ray radiographs centered on the main fracture. Over the next hour precipitates continued to accumulate in fractures as permeability fell by a factor of 2 (Figure 4a) (Carey et al., 2016). Dense precipitates similarly formed within 20 minutes of shearing the second Utica shale (US-02), but permeability changed minimally over the remaining 4 hours of the test. In both cases, BSE/EDS analyses of thin sections cut 45° to the primary shear fractures (see sections 3.1 and 3.2) indicated the precipitates were barium carbonate ($BaCO_3$). Because crystalline witherite occurs

rarely in natural environments, the precipitates could have formed as solid solutions between Ba- and Ca-carbonates during the short experimental time frames (Mavromatis et al., 2016); however, impurities were likely minor because witherite crystal structures can only uptake small amounts of Ca^{2+} due to significant differences in the ionic radii and physicochemical properties of the divalent cations (Astilleros et al., 2000). Additionally, EDS spectra evidenced minor to no calcium in carbonate precipitates.

Precipitation was less abundant in the second Utica shale experiment (US-02) but occurred at a similar rate. As evidenced by Figure 6b, opaque white precipitates began to appear in the middle of the fracture during the first post-shear xCT scan, which was completed within 20 minutes of fracture generation. Precipitates remained stable with increasing confining pressure (steps 5-10 in Figure 6a) and the amount did not change significantly over time, likely because the transition from 180,000 ppm $BaCl_2$ to DI water at about 150 minutes removed the source of Ba^{2+} and pore fluids quickly became undersaturated. The speed of precipitation following initial shearing in both Utica experiments is likely driven by the freshly activated fracture surfaces generated in direct shearing combined with injection of high [Ba^{2+}], which allowed $BaCO_3$ saturation to be achieved with nominal calcite dissolution. Fragments and fault gouge generated in shearing increased the available reactive surface area, which would have directly influenced effective mineral dissolution and precipitation rates,(Gouze & Luquot, 2011) while dissolution of fine grains along the new fractures quickly released CO_3^{2-} that buffered local pH levels and combined with excess [Ba^{2+}] in pore fluids to form $BaCO_3$. The initial batch experiments (Section 2.1) support the need for freshly activated fracture surfaces, as tests revealed precipitates only formed on surfaces that had been roughened right before submerging a shale chip in 2,000 ppm $BaCl_2$ solution (Figure 1b). In this particular system, precipitation may also be accelerated by the fact that the dissolving and precipitating phases were both carbonates, which could lower the degree of supersaturation required to overcome energy barriers for nucleation (Noiriel et al., 2016).

MS-01 confirmed that near-immediate $BaCO_3$ precipitation upon shearing is driven by high levels of [Ba^{2+}], as precipitates only formed with 180,000 ppm $BaCl_2$ in the pore fluid but not after shearing with 200 or 2,000 ppm $BaCl_2$ (at displacements of 0.5 mm and 1 mm, respectively). The lack of precipitation at lower [$BaCl_2$], despite the generation of significant fault gouge and associated reactive surface area in shearing, is consistent with batch testing (see Section 2.1) and stems from low levels of supersaturation. In forsterite carbonation experiments, Giammar et al.(Giammar et al., 2005) similarly found that magnesite nucleation was inhibited below a critical SI. However, the delay in precipitation after raising the injectate [$BaCl_2$] to 180,000 ppm indicates that the process is not solely controlled by fluid saturation but also fracture geometry. No precipitates were observed in the xCT scan collected after the third shear step, which was completed following breakthrough of the 180,000 ppm $BaCl_2$ solution and resulted in further displacement to 1.5 mm (Figure 8b). Roughly an hour later radiographs evidenced brightening at the fracture inlet directly following dynamic shearing, which displaced the sample to 3.2 mm as confining pressure was released from 30 to 5 MPa. Precipitation at the inlet was confirmed in the final xCT scan, collected

after hydroshearing and additional stress-permeability measurements with step changes in confining pressure. Precipitates also formed in other regions of the fracture, but only at narrow choke points where the fracture walls converged. While the fracture is difficult to resolve in the third xCT scan due to limited contrast between the dense $BaCl_2$-rich injectate and shale matrix, the fracture geometry was still relatively clean (i.e. with limited observable fragmentation), which may have limited nucleation. The shear steps that followed resulted in significantly more damage and fault gouge that may have stimulated precipitation by increasing available reactive surface area. In combination, results from the shear tests are consistent with the fact that reaction kinetics depend on both geochemical (i.e. pH, saturation state) and physical (i.e. specific surface area and accessibility of reactive surfaces) conditions.

The discrepancy in the amount of precipitate formed in similar shales that were subjected to the same shearing process may be partially attributable to the difference in carbonate content. Whereas US-01 contained 95% total carbonate (93% calcite and 2% dolomite) with the remainder comprised of quartz, US-02 had 82% calcite and a much higher clay content (10%). The exceptionally high carbonate content in US-01 allowed for rapid dissolution and pH buffering that created favorable conditions for near-immediate precipitation in the freshly formed fractures. As expected, the shale with the lowest initial carbonate content (MS-01) produced the least amount of $BaCO_3$. In this test, precipitation only occurred after intensive shearing that resulted in significant damage in the fracture (Figure 9) and displacement to over 3 mm, whereas the Utica cores were only displaced to ~1 mm before precipitation began. Essentially, because there was less calcite in the Marcellus core, more rock needed to be 'crushed' to expose sufficient reactive surfaces for observable dissolution and precipitation to occur. An additional shear test with 180,000 ppm $BaCl_2$ on a calcite-poor dolomite core, which was excluded from this manuscript for clarity, produced no resolvable precipitates in x-ray radiography and minimal precipitation on fracture surfaces, likely due to the fact that dolomite dissolution kinetics are several orders of magnitude slower than calcite. A lack of precipitation in calcite-limited cores exposed to the same highly concentrated fluids and fractured under the same conditions corroborates that adequate reactive mineral content is necessary for precipitation induced by water-rock interactions. However, the fact that initial batch tests evidenced greater precipitation on marble cores than limestone with the same nearly pure calcite composition indicates that dissolution-precipitation reactions are influenced by other material properties beyond mineralogy that could not be defined in this study. Despite lesser extents of precipitation, both US-02 and MS-01 exhibited non-uniformity in the spatial distribution of $BaCO_3$ analogous to the uneven patterns observed in US-01. Factors driving this trend of strongly localized precipitation along fracture networks are further explored in Section 4.2.

4.2. Localized mineral precipitation

Figures 4(c, d), 6(c, d) and 8(b, c) compare 2D distributions of segmented fracture apertures and precipitates at select stress stages throughout US-02 and MS-01, respectively. The x axis represents distance along the direction of shearing and the z axis along the length of the core, with

the values at each point reflecting the total fracture or precipitate width in the y-direction. Note that the aperture map in US-01 is of limited value because most fractures were filled with precipitates such that dimensions of actual apertures created in shearing are largely unknown.

Given the low permeability and connected porosity of shales that limit fluid accessibility in the bulk matrix, precipitation was limited to the fractures created in direct shearing. This is most clear in 3D renderings of the segmented precipitate and fracture space (see SI), where $BaCO_3$ aligns with the single through-fracture generated in MS-01 and the two oblique through-fractures formed in US-02. Note that precipitation also occurred along the primary shear fracture in US-01 but a 3D segmentation of the fracture network is omitted because, as noted in Section 3.2, most of the original fracture space was filled with precipitates and thus was not captured by the post-reaction scan. The 3D segmentations also highlight differences in reactivity, as precipitation was weakest in the test with the largest fractures and lowest calcite content (MS-01). Precipitates generally formed in small apertures where rock:water ratios and reactive surface area were greatest. In US-02, precipitate segmentation indicated the maximum width of a fracture filled with precipitate was 0.6 mm (Figure 6c). An inverse relationship between saturation index and fracture aperture could be attributable to associated water:rock ratios, where injected Ba^{2+} and dissolved CO_3^{2-} are "diluted" within larger volumes (wide apertures) and concentrated within narrow apertures. Additionally, smaller fluid volumes in narrow fractures are more quickly buffered by $CaCO_3$ dissolution; $BaCO_3$ saturation is more readily achieved at higher pH levels because a greater extent of dissolved inorganic carbon is in the form of carbonate ions (CO_3^{2-}).

While precipitates appeared to fill larger apertures near the inlet in MS-01, the 2D maps are not a perfect representation as multiple narrower fractures stacked orthogonally to the main shear plane are summed and displayed as a single larger aperture. Cross-sections of the final xCT scan reveal that precipitation was strongest at narrow 'choke points' where opposing fracture surfaces came together and weaker along wider fractures, where precipitates occasionally coated the surfaces but did not bridge apertures (Figure 8e). This occurs in part because precipitation favors (and potentially requires) fresh reactive surfaces, which the xCT and SEM data indicated were generally more abundant in narrow choke points created in shear displacement than in wider open fractures characterized by tensile parting. Thin sections confirmed that smaller apertures are generally more favorable for precipitation but are not a complete indicator of where precipitates will form, even when mineralogy and fluid chemistry are relatively homogeneous. As evidenced by the BSE images in Figures 5, 7, and 9, precipitates often completely filled narrow microfractures (<10 μm) but were non-existent or limited to isolated coatings along walls of wider fractures. As noted in Section 4.1 these precipitates likely were not pure witherite but Ca-bearing $BaCO_3$, which has the same orthorhombic crystal structure as aragonite (Astilleros et al., 2000). Precipitates were typically needle-like in structure, similar to observations in batch testing (Section 2.1), and grew orthogonal to fracture walls.

The uneven distributions of precipitates observed in xCT scans and microscale imaging are consistent with previous work linking initial small-scale heterogeneities to localized mineral

reactions and associated structural alterations (Jones & Detwiler, 2016; Menefee et al., 2018; Nogues et al., 2013). Here, precipitates formed non-uniformly in all experiments but followed different patterns of localization along primary flow paths. Precipitation was concentrated near the inlet and outlet of US-01; the fracture interior of US-02; and near the inlet of MS-01. Spatial patterns of precipitation are affected by the rates of local surface reactions relative to fluid transport, which can be quantified by the dimensionless Damköhler number (*Da*), as well as the relationship between advective and diffusive transport (Péclet number, *Pe*). While dimensionless numbers are not quantified here because relevant inputs (e.g. flow velocities and reaction rates) are highly variable and uncertain throughout the complex geometry of the shear-induced microfractures where *Pe* and *Da* would be of interest, some of the general trends observed in this work are consistent with prior studies that evaluated dimensionless numbers in more well-constrained systems. Detwiler observed that low *Da* (i.e., reaction kinetics are slow relative to advective transport) led to uniform mineral dissolution but high *Da* promoted channelization, leaving outlying regions of the fracture unexposed to injected fluids (Detwiler, 2008). A recent study also found that the extent of preferential dissolution increased with increasing heterogeneities in velocity and mineral distributions in carbonate-rich cores (Al-Khulaifi et al., 2019). In lattice-Boltzmann simulations on simplified porous media, Kang et al. showed that under higher Péclet and Damköhler numbers (i.e., advective conditions), precipitates first clog smaller fractures and decrease with distance from the fluid inlet (Kang et al., 2003). Noiriel et al. also found that column-scale precipitation rates depend strongly on saturation index, which is greatest near column inlets (Noiriel et al., 2016). These findings are consistent with the general trends observed along primary shear fractures in US-01 and MS-01, where preferential precipitation near the inlet indicates dissolution proceeded quickly upon contact with high-[$BaCl_2$] fluids and precipitates nucleated once a critical supersaturation threshold was achieved. Non-uniform precipitation was also likely influenced by non-uniform flow, where inaccessible regions were devoid of precipitates because the injected fluid was the only source of barium in the system.

In this study, strong precipitate localization observed in all tests resulted from heterogeneities in mineral composition and distribution; local pore fluid saturation; reactive surface areas of exposed grains; and fracture roughness and microstructure. BSE analyses indicated $BaCO_3$ formed almost exclusively on $CaCO_3$, which was the primary carbonate source in the host rocks and exhibits dissolution kinetics orders of magnitude faster than other minerals (e.g. clay, quartz) in the shale matrices. Previous work has shown similar preferential nucleation of secondary phases occurs on the primary reactive minerals that contribute key constituent cations and is most pronounced in low-flow zones where transport is primarily controlled by diffusion (Menefee et al., 2017, 2018). Jones and Detwiler also demonstrated that mineral heterogeneities can promote localized precipitation-induced aperture reductions, channeling flow into regions with lower reactivity (Jones & Detwiler, 2016). Here, rapid precipitation in the most reactive regions may have similarly diverted flow and slowed reaction progress, preventing further growth and accumulation of precipitates. In addition to preferential precipitation on reactive minerals, thin section analyses confirmed that precipitation was generally more favorable in more heavily sheared regions with

extensive microfractures and fragmentation, but in many of these regions precipitates effectively cemented some fragments or fractures while not forming on adjacent ones (e.g. Figure 9).

Mineralogical and structural variations combined with transport limitations likely created or enhanced small-scale chemical heterogeneities with respect to saturation indices. Localized $CaCO_3$ dissolution promotes rapid pH buffering given the fast reaction kinetics of $CaCO_3$, but similarly rapid $BaCO_3$ precipitation could quickly consume released carbonate ions and neutralize surrounding fluids, precluding further $BaCO_3$ nucleation in adjacent regions with lower reactivity despite abundant Ba^{2+} in the pore fluid. In combination, mineralogical heterogeneities inherent to the core and structural heterogeneities generated during shearing create spatial inconsistencies in properties such as reactive surface area and saturation states, which in turn strongly impact precipitation kinetics. Even in homogeneous mineral systems, actual precipitation rates along fracture walls may vary in response to changes in conditions such as pressure, pore fluid composition, and the morphology of underlying mineral surfaces (Noiriel et al., 2016). It is unclear how precipitate localization observed here would translate to similar mineralogies at reservoir scales, as previous work has suggested the significance of mineral spatial distributions diminishes when reactive minerals are abundant in bulk (Li et al., 2007). However, the idiosyncratic trend of precipitates forming haphazardly throughout fracture networks despite a relatively uniform thermodynamic drive highlights the challenges associated with predicting precipitation reactions even when reservoir conditions are well constrained.

4.3. Precipitation-induced permeability alterations

The initial permeability of the intact samples was immeasurable (<1 μD). After sample failure in the first Utica experiment (US-01), permeability increased near-instantaneously to 0.25 mD; fell slightly over the next 15 minutes as axial stress was held over 60 MPa; and peaked at 0.43 mD upon return to isotropic stress conditions at 3.5 MPa (Section 3.2). Over the remainder of the experiment, permeability decreased by 80% relative to its peak. Most of this reduction occurred within the first hour after initial shearing, concomitant with progressive infilling of precipitates within the fracture that was evidenced by the growth and intensification of bright regions in radiographs aligned with the shear plane. While the direct effects of precipitates on fracture permeability could not be delineated due to simultaneous changes in isotropic pressure, analysis of the post-reaction xCT scan indicates that precipitation filled substantial portions of the fracture network and likely obstructed fluid transport (Figures 4d and 4e). Extrapolation of the tail of the permeability curve indicated it would take roughly 45 hours for permeability to fall below 1 μD, which would essentially seal the fracture network.

In contrast to the notable permeability reductions observed in US-01, precipitation in the second Utica experiment (US-02) was less extensive and failed to definitively impact fluid transport. The rapid precipitation evidenced in xCT scans acquired directly after shearing may have contributed to the permeability reduction between 75 and 150 minutes (Figure 6a). Additionally, the select fracture filling observed in xCT scans could drive local permeability reductions that were

not captured in bulk measurements across the entire specimen. Precipitate volumes and fracture permeability remained relatively stable for the remainder of the test, which involved a series of stepwise increases in effective stress as DI water continued to flow through the core. The 3D videos (see SI, videos S1-S3) highlight how precipitation led to conflicting permeability trends between the two Utica experiments; whereas smaller and more isolated pockets of $BaCO_3$ formed in US-02, leaving pathways open to continued injection, the abundance of precipitation along the entirety of the main fracture in US-01 would be expected to restrict flow.

In the final test, permeability increased following the initial direct shear steps (peaking around 280 mD) but dropped below 1 μD during the fourth shear (dynamic shearing). The third and fourth shear steps were both conducted with 18 weight percent $BaCl_2$ in the pore fluid but it is unclear whether the permeability reductions were attributable to precipitation, particularly near the fluid inlet; clay mobilization and clogging; or changes in fracture geometry, such as compaction of asperities. While the final xCT scan revealed precipitates filling the fracture inlet, the exact timing of precipitation relative to permeability changes in MS-01 is unclear given that over 2 hours elapsed between the penultimate and final scans with multiple changes in direct shear and confining stress along with a switch to more dilute pore fluid (200 ppm $BaCl_2$) following hydroshearing (~180 minutes). However, the fact that these precipitates appeared in radiographs around the time of the permeability decline observed during dynamic shearing indicates they may have contributed to restricted flow, similar to the permeability reductions associated with precipitate accumulation at the fracture inlet and outlet in US-01. Although the overall extent of $BaCO_3$ was lowest in this experiment, preferential precipitation near the inlet could have resulted in a greater impact on permeability than the more dispersed precipitation in US-02.

While this study focused on how precipitation affects permeability, the rate and extent of precipitation may be correlated with initial fracture permeability. Following shear failure, permeability peaked around 0.43 mD in US-01 compared with 235 mD in US-02 and 280 mD in MS-01. The less apparent changes to permeability in US-02 and MS-01 may partly be a consequence of the high fracture permeability, which might require more precipitation to cause a significant change in permeability. The permeability values are consistent with observed differences in fracture apertures, which were smallest in US-01 (generally <0.3 mm in segmented fractures not filled with precipitates). In addition to larger average apertures, the mm-scale fracture network in US-02 was more extensive with two oblique fractures that spanned the entire length of the core. MS-01 only produced one main shear fracture but apertures were much larger, averaging ~1 mm parallel to the flow direction. Considering that precipitates formed preferentially where fracture walls converged in US-02 and MS-01, the narrow initial shear fractures created in US-01 likely established favorable conditions for precipitation along the entire fracture rather than at intermittent fracture constrictions.

4.4. 4D fracture and precipitate evolution

While the focus of this study was on geochemical reactions, US-02 concomitantly tested fracture evolution under increasing effective stress states. Total fracture and precipitate volumes across the core, calculated from the segmented xCT datasets (section 2.4), are plotted as a function of confining stress in Figure 10. Quantitatively, the total fracture volume across the core decreased by a factor of 4 from initial shearing at 3.5 MPa to the final step at 30 MPa while precipitate volumes changed minimally; the slight apparent rise in precipitation in Figure 10 is consistent with variations in scan quality rather than a reflection of active precipitate growth. Visually, the near-immediate precipitation observed upon shearing with high-$BaCl_2$ fluid was followed by minimal growth for the duration of the experiment (Figure 6c), while fracture apertures notably closed with increasing confining stress (Figure 6d). Most changes occurred in narrower fractures, which visibly decreased in aperture with increasing stress and in some areas were essentially closed (i.e., apertures fell below the voxel resolution) by 30 MPa. As discussed in Section 4.2, narrow fractures were also where the majority of precipitation occurred. In actual systems where precipitates progressively accumulate due to continued exposure to reactive fluids, increasing stress could accelerate fracture sealing by mechanically reducing apertures as they are simultaneously filled with precipitates.

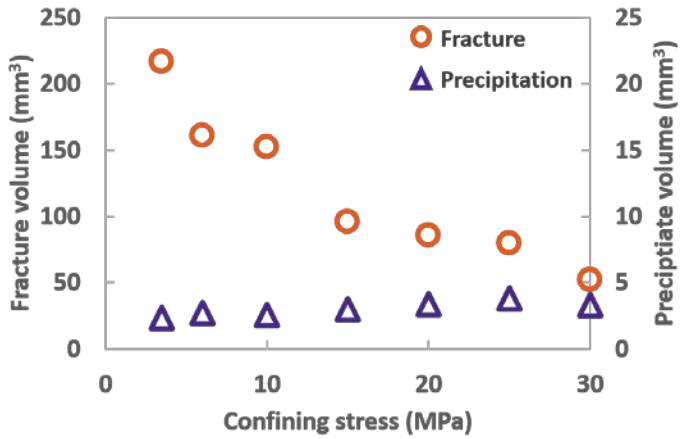

Figure 10. Changes in total fracture and precipitate volumes as a function of confining stress in US-02. Volumes were summed across the entire core based on segmented xCT datasets for each confining step.

Despite narrowing apertures and active precipitation, permeability did not decrease significantly in this test (Figure 5a). The dense precipitates may have served as proppants in some regions, creating effective asperities that resisted complete fracture closure. Prior work has demonstrated that secondary minerals can form in porous layers along fracture walls that prop open fractures without completely blocking fluid access (Lisabeth et al., 2017). In percolation experiments subjecting pre-fractured quartz-monzonite samples to calcite-saturated fluid, Aben et al. similarly found that calcite precipitation reduced fracture volume but negligibly affected permeability (Aben et al., 2017). This was primarily due to the fact that most precipitation occurred in sheltered regions downstream of flow barriers such as fracture steps, kinks, and asperities,

leaving main channels unobstructed, while calcite crystals replaced or supported asperities once they grew large enough to span fracture walls (Aben et al., 2017). In addition to location, the ability of secondary precipitates to maintain fracture permeability or structural integrity will depend on their ability to resist re-dissolution and relative rates of dissolution of primary minerals. After injecting synthetic hydraulic fracturing fluid through a Marcellus shale core without acid, Vankeuren et al. reported that the absence of acid-induced calcite dissolution resulted in net fracture volume reductions due to mixing-induced barite precipitation, which could either constrict flow or complement proppants to maintain fracture apertures over longer time frames (Vankeuren et al., 2017). Conversely, dissolution in excess of precipitation can lead to asperity removal and fracture compaction (Ellis et al., 2013; Elsworth & Yasuhara, 2010) or channelization and fracture opening (Deng & Peters, 2019; Luquot & Gouze, 2009). In addition to competing reactions, precipitates could be impacted by changes in environmental conditions such as temperature and pressure swings that were not explicitly evaluated in this study. While all experiments were conducted ~20°C, calcite exhibits retrograde solubility and thus may be more resistant to dissolution at the higher temperatures anticipated in most target reservoirs (50-70°C), while increasing $BaCO_3$ solubility with temperature could temper the speed and extent of precipitation observed in our low-temperature experiments. On the other hand, carbonate reaction kinetics increase with temperature, which could accelerate the rate and extent of both $CaCO_3$ dissolution and $BaCO_3$ precipitation in the system considered here. More generally, temperature-dependent mineral properties (e.g. solubility, reaction kinetics) will influence both the propensity of a secondary phase to form and its resistance to deformation over time. Further work is necessary to define conditions under which new precipitates are sufficiently recalcitrant to improve fracture stability (e.g. by counteracting asperity dissolution or mechanical compaction) and understand the geomechanical implications of competing geochemical processes under a range of reservoir conditions.

4.5. Implications for multi-scale modeling

Results from this work underscore several challenges associated with modeling reactive subsurface systems. As discussed in Section 4.2, key determinants of dissolution-precipitation reactions (e.g. specific surface area, surface reactivity, saturation index) are subject to strongly localized variations that are nearly impossible to resolve in complex microfracture networks. Prior work has also shown that detailed knowledge of fracture geometry is necessary to accurately calculate permeability and flow,(Olson et al., 2007) but sufficient resolution of apertures and mineral composition, particularly at fracture intersections, is difficult to achieve with realistic computational efficiency. Even if aperture distributions and geochemical conditions are well-constrained, our experiments demonstrate precipitation can occur inconsistently despite relatively uniform thermodynamic drive, which further complicates application of simulation results. This was evidenced in 1D reactive transport models that were developed here to complement experimental results but ultimately omitted from this study because they added complexity with marginal utility. The 1D models failed to capture observed heterogeneities in precipitation patterns,

predicting secondary minerals would automatically form where they were thermodynamically and kinetically favorable. This limitation stems partly from oversimplifications necessary to achieve computational efficiency in the simulations, such as distilling rough and complex fracture surfaces into single apertures and relying on published data for individual minerals that may not directly translate to heterogeneous systems. Integrating reactive transport and geomechanics into models from pore to continuum scales remains an open challenge in precipitation-dominated systems.

As discussed in the introduction, low-permeability formations rely on fracture flow rather than matrix flow and thus the location of precipitates (e.g., in dead-end zones vs. critical pore throats) along with the extent to which they coat or bridge fracture surfaces will drive long-term permeability changes that may inhibit fluid injection or production. In addition, precipitation on fracture walls may modify matrix-fracture communication, perhaps limiting transport of chemical or thermal constituents into the fracture network. To date, dissolution-precipitation reactions have been incorporated into pore network models to evaluate porosity-permeability evolution(Nogues et al., 2013) but the resulting redistribution of mineral mass throughout fracture networks has not been fully captured in modeling efforts (Elsworth & Yasuhara, 2010). Yasuhara et al. developed mechanistic models describing compaction of loose quartz aggregates that account for mass redistribution via dissolution between grains, diffusion from grain interfaces to pores, and precipitation on free faces and found that the dominant processes evolve with interconnected changes in stress, pore space, and grain contact area (Yasuhara, 2003). Subsequent models of these processes in idealized fractures were validated with observational data from flow-through experiments on novaculite and limestone, but multiple fitting parameters were adjusted to achieve reasonable fits to experimental changes in apertures and effluent chemistry (Elsworth & Yasuhara, 2010). In our study, simulations would fail to predict the location of all precipitation reactions because two adjacent microfractures with equivalent apertures and geochemical conditions could exhibit conflicting behavior with respect to actual formation of precipitates. Effectively capturing spatial distributions of precipitates is extremely challenging without forcing or overly constraining input parameters, which diminishes the utility of the model by limiting applications to other systems or extensions to greater spatial and temporal scales. The latter may be the most significant issue, as challenges associated with anticipating or even retroactively evaluating non-uniform precipitation at core scales will be exacerbated when extending modeling efforts to larger systems. Even if precipitation patterns can be effectively predicted at scale, the implications may be unclear, as different precipitates may have different effects on permeability depending on their unique crystal habit, but mineral-specific data necessary to improve precipitation-permeability relationships are limited (Xie et al., 2015). While upscaling our core-scale results was beyond the scope of this study, prior work has indicated that pore-scale spatial heterogeneities in chemical and physical properties will impact continuum-scale reaction kinetics and need to be considered in reservoir models to more accurately predict precipitate localization (Li et al., 2006).

Conclusions

This study highlights the challenges associated with predicting geochemical reactions and consequent alterations in subsurface reservoirs exposed to reactive fluids. Optimizing experimental conditions for secondary mineralization resulted in rapid precipitation due to a combination of fast reaction kinetics, which were accelerated by high reactive surface areas generated in direct shearing, and artificially high levels of supersaturation that reduced nucleation energy barriers. In the most reactive system, precipitates quickly filled narrow apertures and blocked fluid transport sufficiently to reduce permeability by ~80% within hours of shear fracturing. The extent of precipitation in three different experiments presented here decreased with decreasing carbonate ($CaCO_3$) content in the shale matrix, but all experiments exhibited strong precipitate localization due to feedback among mineralogical, geochemical, and structural heterogeneities either inherent to the host rock or created during shear. Spatial distributions of precipitates are critical in low-permeability shales that rely on fractures for fluid flow, as even small volumes of precipitates can have pronounced impacts on long-term transport and injectivity if they coat fracture walls, form in narrow pore throats, or occur along critical flow paths.

Whereas most related experimental studies have focused on mixing-induced precipitation resulting from introduction of incompatible fluids, such as when barite scale forms following injection of sulfate-rich fluids into barium-rich reservoir fluids, we demonstrate that interactions between fluids and the surrounding rock are also significant factors in precipitation reactions but are objectively more difficult to predict and prevent. As such, subsurface fluid-rock interactions that have not been rigorously characterized at the pore- and core-scale are often oversimplified or overlooked in reservoir-scale modeling efforts. At the core scale, discrepancies in the timing, extent, and distribution of precipitates formed in similar shales during these experiments reflect lingering idiosyncrasies associated with precipitation processes. Even when a secondary mineral is thermodynamically and kinetically favored to form throughout a given system, its nucleation and growth may be highly localized and depends on complex and dynamic feedback among geophysical and geochemical conditions that cannot be predicted *a priori*. Furthermore, where precipitates do form, resulting impacts on fluid transport and accessibility are driven by interconnected alterations to porosity, permeability, and grain size distributions. While this work focused on the role of geochemical reactions, geomechanical factors will also control the impact of precipitation on fluid transport through fracture systems. For example, Frash et al. (2018) discuss several factors governing changes in fracture permeability including changing stress conditions and fracture reactivation but also emphasized that the behavior of fractures depended on the stress at which fractures were originally generated.

In a broader context, these results contribute to our understanding of how fractures respond to geochemical alterations under subsurface stress conditions. Precipitation reactions are still poorly understood but play key roles, both positive and negative, in efficient reservoir exploitation for existing and emerging energy applications. Most intuitively, sufficient quantities of precipitates can limit reservoir injectivity or productivity by clogging fractures and blocking critical fluid flow paths. However, precipitates can be desirable in applications such as geologic carbon storage, where CO_2

trapping through mineralization represents the most secure and permanent form of carbon sequestration (Matter & Kelemen, 2009). Precipitation can also be leveraged for targeted permeability reduction in operations where fluid migration needs to be actively controlled, such as geologic carbon storage and enhanced geothermal energy production (Plattenberger et al., 2019). While our experiments indicated highly reactive reservoirs can promote sudden and extensive precipitation in the presence of reactive fluids that may lead to fracture sealing, observations also suggested that localized precipitates in less reactive systems can serve as effectual proppants that prevent compaction-driven fracture closure with increasing stress without completely sealing fractures from further flow. The rapid precipitation reactions observed here could also serve as analogs to natural systems where the ability of precipitates to counteract fracture sealing requires near-immediate rates of crystallization because closure stresses act instantaneously. Further work is needed to more thoroughly define conditions under which precipitates serve to maintain permeability, by propping or even propagating fractures, or reduce permeability through pore clogging and fracture sealing.

Acknowledgements

This work (released under LA-UR-19-32157) was supported by a U.S. Department of Energy Office of Science Graduate Student Research (SCGSR) award from 2018 Solicitation 1 and in part by a National Science Foundation Graduate Research Fellowship under Grant No. DGE 1256260. Los Alamos work was supported by the Department of Energy (DOE) Basic Energy Sciences program (LANLE3W1). Additional support was provided by an appointment from the National Energy Technology Laboratory Research Participation Program, sponsored by the U.S. Department of Energy and administered by the Oak Ridge Institute for Science. Supporting x-ray computed tomography data used in the production of this manuscript are available through the Digital Rocks Portal at https://doi.org/10.17612/S0FM-NP04.

References

Aben, F. M., Doan, M.-L., Gratier, J.-P., & Renard, F. (2017). Experimental postseismic recovery of fractured rocks assisted by calcite sealing: Experimental recovery of fractured rocks. *Geophysical Research Letters*, *44*(14), 7228–7238. https://doi.org/10.1002/2017GL073965

Al-Khulaifi, Y., Lin, Q., Blunt, M. J., & Bijeljic, B. (2019). Pore-Scale Dissolution by CO_2-Saturated Brine in a Multimineral Carbonate at Reservoir Conditions: Impact of Physical and Chemical Heterogeneity. *Water Resources Research*, *55*(4), 3171–3193. https://doi.org/10.1029/2018WR024137

Astilleros, J. M., Pina, C. M., Fernández-Dıaz, L., & Putnis, A. (2000). The effect of barium on calcite 1014 surfaces during growth. *Geochimica et Cosmochimica Acta*, *64*(17), 2965–2972.

Beckingham, L. E. (2017). Evaluation of Macroscopic Porosity-Permeability Relationships in Heterogeneous Mineral Dissolution and Precipitation Scenarios: Evaluation of Permeability Relationships. *Water Resources Research*, *53*(12), 10217–10230. https://doi.org/10.1002/2017WR021306

Carey, J. W., Rougier, E., Lei, Z., & Viswanathan, H. (2015). Experimental investigation of fracturing of shale with water. In *49th US Rock Mechanics/Geomechanics Symposium*. American Rock Mechanics Association.

Carey, J. W., Lei, Z., Rougier, E., Mori, H., & Viswanathan, H. (2015). Fracture-permeability behavior of shale. *Journal of Unconventional Oil and Gas Resources*, *11*, 27–43. https://doi.org/10.1016/j.juogr.2015.04.003

Carey, J. W., Frash, L. P., Viswanathan, H. S., & others. (2016). Dynamic triaxial study of direct shear fracturing and precipitation-induced transient permeability observed by in situ x-ray radiography. In *50th US Rock Mechanics/Geomechanics Symposium*. American Rock Mechanics Association. Retrieved from https://www.onepetro.org/conference-paper/ARMA-2016-566

Deng, H., & Peters, C. A. (2019). Reactive Transport Simulation of Fracture Channelization and Transmissivity Evolution. *Environmental Engineering Science*, *36*(1), 90–101. https://doi.org/10.1089/ees.2018.0244

Deng, H., Steefel, C., Molins, S., & DePaolo, D. (2018). Fracture Evolution in Multimineral Systems: The Role of Mineral Composition, Flow Rate, and Fracture Aperture Heterogeneity. *ACS Earth and Space Chemistry*, *2*(2), 112–124. https://doi.org/10.1021/acsearthspacechem.7b00130

Detwiler, R. L. (2008). Experimental observations of deformation caused by mineral dissolution in variable-aperture fractures: Dissolution and Deformation in Fractures. *Journal of Geophysical Research: Solid Earth*, *113*(B8). https://doi.org/10.1029/2008JB005697

Ellis, B. R., Fitts, J. P., Bromhal, G. S., McIntyre, D. L., Tappero, R., & Peters, C. A. (2013). Dissolution-driven permeability reduction of a fractured carbonate caprock. *Environmental Engineering Science*, *30*(4), 187–193. https://doi.org/10.1089/ees.2012.0337

Elsworth, D., & Yasuhara, H. (2010). Mechanical and transport constitutive models for fractures subject to dissolution and precipitation. *International Journal for Numerical and Analytical Methods in Geomechanics*, *34*(5), 533–549. https://doi.org/10.1002/nag.831

Emmanuel, S., & Berkowitz, B. (2005). Mixing-induced precipitation and porosity evolution in porous media. *Advances in Water Resources*, *28*(4), 337–344. https://doi.org/10.1016/j.advwatres.2004.11.010

Emmanuel, S., Ague, J. J., & Walderhaug, O. (2010). Interfacial energy effects and the evolution of pore size distributions during quartz precipitation in sandstone. *Geochimica et Cosmochimica Acta*, *74*(12), 3539–3552. https://doi.org/10.1016/j.gca.2010.03.019

Frash, L., Carey, J. W., Ickes, T. L., Porter, M. L., & Viswanathan, H. S. (2018). *Permeability of fractures created by triaxial direct shear and simultaneous x-ray imaging*. Los Alamos National Lab.(LANL), Los Alamos, NM (United States).

Frash, L. P. (2016). *DIsco*. Los Alamos National Laboratory: Richard P. Feynman Center for Innovation: Los Alamos National Laboratory: Richard P. Feynman Center for Innovation.

Frash, L. P., Carey, J. W., Lei, Z., Rougier, E., Ickes, T., & Viswanathan, H. S. (2016). High-stress triaxial direct-shear fracturing of Utica shale and in situ X-ray microtomography with permeability measurement: SHALE FRACTURE, μCT, AND PERMEABILITY. *Journal of Geophysical Research: Solid Earth*, *121*(7), 5493–5508. https://doi.org/10.1002/2016JB012850

Frash, L. P., Carey, J. W., & Welch, N. J. (2019). Scalable En Echelon Shear-Fracture Aperture-Roughness Mechanism: Theory, Validation, and Implications. *Journal of Geophysical Research: Solid Earth*, *124*(1), 957–977. https://doi.org/10.1029/2018JB016525

Garing, C., Gouze, P., Kassab, M., Riva, M., & Guadagnini, A. (2015). Anti-correlated Porosity–Permeability Changes During the Dissolution of Carbonate Rocks: Experimental Evidences and Modeling. *Transport in Porous Media*, *107*(2), 595–621. https://doi.org/10.1007/s11242-015-0456-2

Giammar, D. E., Bruant, R. G., & Peters, C. A. (2005). Forsterite dissolution and magnesite precipitation at conditions relevant for deep saline aquifer storage and sequestration of carbon dioxide. *Chemical Geology*, *217*(3–4), 257–276. https://doi.org/10.1016/j.chemgeo.2004.12.013

Gouze, P., & Luquot, L. (2011). X-ray microtomography characterization of porosity, permeability and reactive surface changes during dissolution. *Journal of Contaminant Hydrology*, *120–121*, 45–55. https://doi.org/10.1016/j.jconhyd.2010.07.004

Huerta, N. J., Hesse, M. A., Bryant, S. L., Strazisar, B. R., & Lopano, C. L. (2013). Experimental evidence for self-limiting reactive flow through a fractured cement core: Implications for time-dependent wellbore leakage. *Environmental Science & Technology*, *47*(1), 269–275. https://doi.org/10.1021/es3013003

Jones, T. A., & Detwiler, R. L. (2016). Fracture sealing by mineral precipitation: The role of small-scale mineral heterogeneity: Mineral Precipitation in Fractures. *Geophysical Research Letters*, *43*(14), 7564–7571. https://doi.org/10.1002/2016GL069598

Kang, Q., Zhang, D., & Chen, S. (2003). Simulation of dissolution and precipitation in porous media: Dissolution and Precipitation in Porous Media. *Journal of Geophysical Research: Solid Earth*, *108*(B10). https://doi.org/10.1029/2003JB002504

Li, L., Peters, C. A., & Celia, M. A. (2007). Effects of mineral spatial distribution on reaction rates in porous media. *Water Resources Research*, *43*(1), n/a-n/a. https://doi.org/10.1029/2005WR004848

Li, L., Peters, C. A., & Celia, M. A. (2006). Upscaling geochemical reaction rates using pore-scale network modeling. *Advances in Water Resources*, *29*(9), 1351–1370. https://doi.org/10.1016/j.advwatres.2005.10.011

Lisabeth, H. P., Zhu, W., Kelemen, P. B., & Ilgen, A. (2017). Experimental evidence for chemo-mechanical coupling during carbon mineralization in ultramafic rocks. *Earth and Planetary Science Letters*, *474*, 355–367. https://doi.org/10.1016/j.epsl.2017.06.045

Luhmann, A. J., Tutolo, B. M., Bagley, B. C., Mildner, D. F. R., Seyfried, W. E., & Saar, M. O. (2017). Permeability, porosity, and mineral surface area changes in basalt cores induced by reactive transport of CO_2-rich brine: Physical changes from reaction in basalt. *Water Resources Research*, *53*(3), 1908–1927. https://doi.org/10.1002/2016WR019216

Luquot, L., & Gouze, P. (2009). Experimental determination of porosity and permeability changes induced by injection of CO2 into carbonate rocks. *Chemical Geology*, *265*(1–2), 148–159. https://doi.org/10.1016/j.chemgeo.2009.03.028

Matter, J. M., & Kelemen, P. B. (2009). Permanent storage of carbon dioxide in geological reservoirs by mineral carbonation. *Nature Geoscience*, *2*(12), 837–841. https://doi.org/10.1038/ngeo683

Mavromatis, V., van Zuilen, K., Purgstaller, B., Baldermann, A., Nägler, T. F., & Dietzel, M. (2016). Barium Isotope Fractionation during Witherite (BaCO3) Dissolution, Precipitation and at Equilibrium. *Geochimica et Cosmochimica Acta*, *190*, 72–84. https://doi.org/10.1016/j.gca.2016.06.024

McGuire, T. P., Elsworth, D., & Karcz, Z. (2013). Experimental Measurements of Stress and Chemical Controls on the Evolution of Fracture Permeability. *Transport in Porous Media*, *98*(1), 15–34. https://doi.org/10.1007/s11242-013-0123-4

Menefee, A. H., Li, P., Giammar, D. E., & Ellis, B. R. (2017). Roles of transport limitations and mineral heterogeneity in carbonation of fractured basalts. *Environmental Science & Technology*, *51*(16), 9352–9362. https://doi.org/10.1021/acs.est.7b00326

Menefee, A. H., Giammar, D. E., & Ellis, B. R. (2018). Permanent CO_2 Trapping through Localized and Chemical Gradient-Driven Basalt Carbonation. *Environmental Science & Technology*, *52*(15), 8954–8964. https://doi.org/10.1021/acs.est.8b01814

Nogues, J. P., Fitts, J. P., Celia, M. A., & Peters, C. A. (2013). Permeability evolution due to dissolution and precipitation of carbonates using reactive transport modeling in pore networks. *Water Resources Research*, *49*(9), 6006–6021. https://doi.org/10.1002/wrcr.20486

Noiriel, C. (2004). Investigation of porosity and permeability effects from microstructure changes during limestone dissolution. *Geophysical Research Letters*, *31*(24). https://doi.org/10.1029/2004GL021572

Noiriel, C., Renard, F., Doan, M.-L., & Gratier, J.-P. (2010). Intense fracturing and fracture sealing induced by mineral growth in porous rocks. *Chemical Geology*, *269*(3–4), 197–209. https://doi.org/10.1016/j.chemgeo.2009.09.018

Noiriel, C., Gouze, P., & Madé, B. (2013). 3D analysis of geometry and flow changes in a limestone fracture during dissolution. *Journal of Hydrology*, *486*, 211–223. https://doi.org/10.1016/j.jhydrol.2013.01.035

Noiriel, C., Steefel, C. I., Yang, L., & Bernard, D. (2016). Effects of pore-scale precipitation on permeability and flow. *Advances in Water Resources*, *95*, 125–137. https://doi.org/10.1016/j.advwatres.2015.11.013

Olson, J. E., Laubach, S. E., & Lander, R. H. (2007). Combining diagenesis and mechanics to quantify fracture aperture distributions and fracture pattern permeability. *Geological Society, London, Special Publications*, *270*(1), 101–116.

Peuble, S., Godard, M., Luquot, L., Andreani, M., Martinez, I., & Gouze, P. (2015). CO_2 geological storage in olivine rich basaltic aquifers: New insights from reactive-percolation experiments. *Applied Geochemistry*, *52*, 174–190. https://doi.org/10.1016/j.apgeochem.2014.11.024

Plattenberger, D. A., Ling, F. T., Peters, C. A., & Clarens, A. F. (2019). Targeted Permeability Control in the Subsurface via Calcium Silicate Carbonation. *Environmental Science & Technology*, *53*(12), 7136–7144. https://doi.org/10.1021/acs.est.9b00707

Polak, A., Elsworth, D., Liu, J., & Grader, A. S. (2004). Spontaneous switching of permeability changes in a limestone fracture with net dissolution: Spontaneous Switching of Permeability Changes. *Water Resources Research*, *40*(3). https://doi.org/10.1029/2003WR002717

Pruess, K., & Müller, N. (2009). Formation dry-out from CO_2 injection into saline aquifers: 1. Effects of solids precipitation and their mitigation. *Water Resources Research*, *45*(3). https://doi.org/10.1029/2008WR007101

Pyrak-Nolte, L. J., DePaolo, D. J., & Pietra, T. (2015). *Controlling subsurface fractures and fluid flow: a basic research agenda*. USDOE Office of Science (SC)(United States).

Steefel, C. I., Appelo, C. A. J., Arora, B., Jacques, D., Kalbacher, T., Kolditz, O., et al. (2015). Reactive transport codes for subsurface environmental simulation. *Computational Geosciences*, *19*(3), 445–478. https://doi.org/10.1007/s10596-014-9443-x

Tartakovsky, A. M., Redden, G., Lichtner, P. C., Scheibe, T. D., & Meakin, P. (2008). Mixing-induced precipitation: Experimental study and multiscale numerical analysis: Mixing-induced Precipitation. *Water Resources Research*, *44*(6). https://doi.org/10.1029/2006WR005725

Vankeuren, A. N. (P)., Hakala, J. A., Jarvis, K., & Moore, J. E. (2017). Mineral Reactions in Shale Gas Reservoirs: Barite Scale Formation from Reusing Produced Water As Hydraulic Fracturing Fluid. *Environmental Science & Technology*, *51*(16), 9391–9402. https://doi.org/10.1021/acs.est.7b01979

Walsh, S. D. C., Du Frane, W. L., Mason, H. E., & Carroll, S. A. (2013). Permeability of Wellbore-Cement Fractures Following Degradation by Carbonated Brine. *Rock Mechanics and Rock Engineering*, *46*(3), 455–464. https://doi.org/10.1007/s00603-012-0336-9

Weng, X., Chuprakov, D., Kresse, O., Prioul, R., & Wang, H. (2018). Hydraulic fracture-height containment by permeable weak bedding interfaces. *GEOPHYSICS*, *83*(3), MR137–MR152. https://doi.org/10.1190/geo2017-0048.1

Wildenschild, D., & Sheppard, A. P. (2013). X-ray imaging and analysis techniques for quantifying pore-scale structure and processes in subsurface porous medium systems. *Advances in Water Resources*, *51*, 217–246. https://doi.org/10.1016/j.advwatres.2012.07.018

Xie, M., Mayer, K. U., Claret, F., Alt-Epping, P., Jacques, D., Steefel, C., et al. (2015). Implementation and evaluation of permeability-porosity and tortuosity-porosity relationships linked to mineral dissolution-precipitation. *Computational Geosciences*, *19*(3), 655–671. https://doi.org/10.1007/s10596-014-9458-3

Yasuhara, H. (2003). A mechanistic model for compaction of granular aggregates moderated by pressure solution. *Journal of Geophysical Research*, *108*(B11). https://doi.org/10.1029/2003JB002536

Yasuhara, H., & Elsworth, D. (2008). Compaction of a Rock Fracture Moderated by Competing Roles of Stress Corrosion and Pressure Solution. *Pure and Applied Geophysics*, *165*(7), 1289–1306. https://doi.org/10.1007/s00024-008-0356-2

Zhang, C., Dehoff, K., Hess, N., Oostrom, M., Wietsma, T. W., Valocchi, A. J., et al. (2010). Pore-Scale Study of Transverse Mixing Induced $CaCO_3$ Precipitation and Permeability Reduction in a Model Subsurface Sedimentary System. *Environmental Science & Technology*, *44*(20), 7833–7838. https://doi.org/10.1021/es1019788

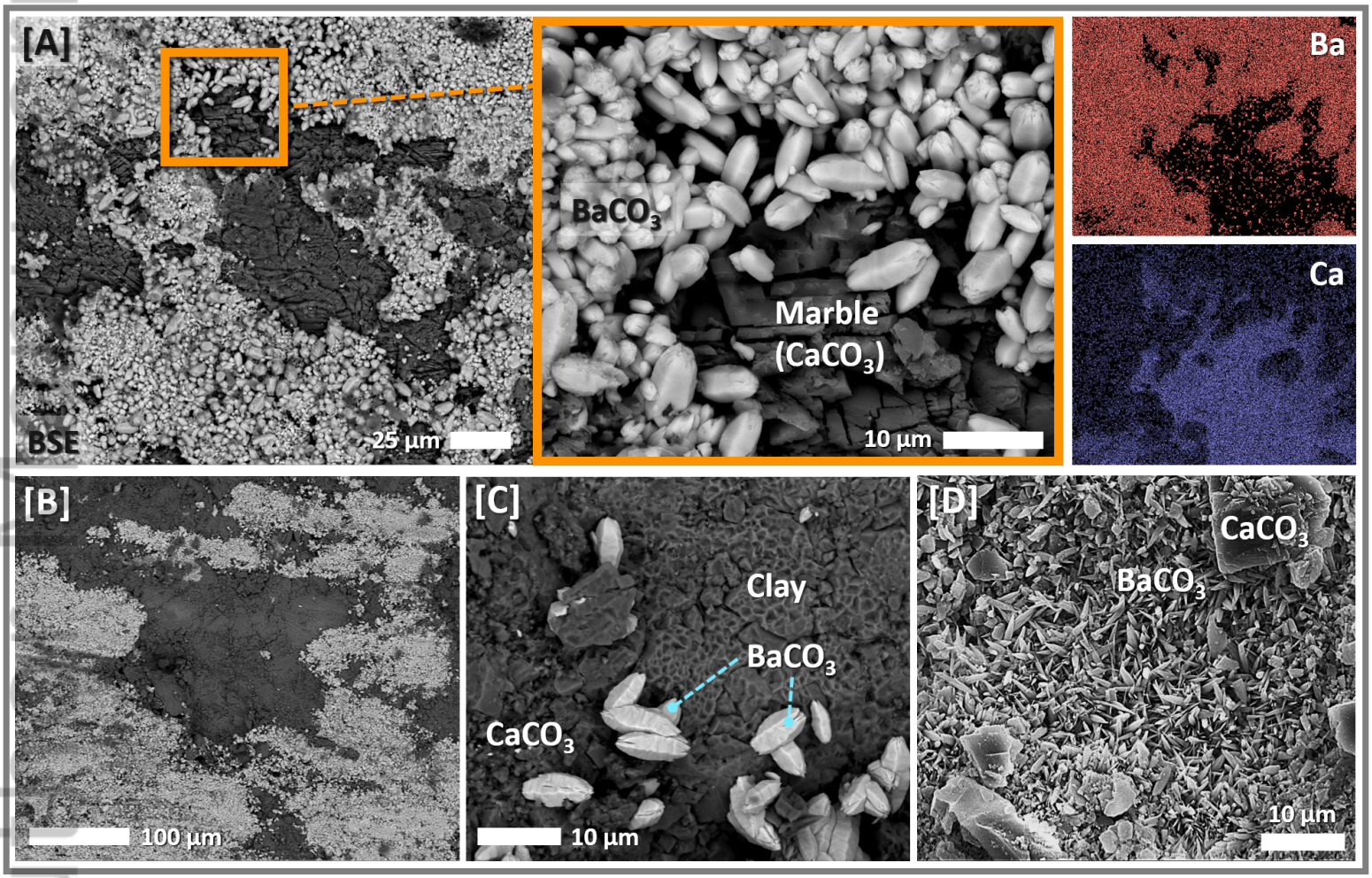

2019JB018864-f01-z-.tif

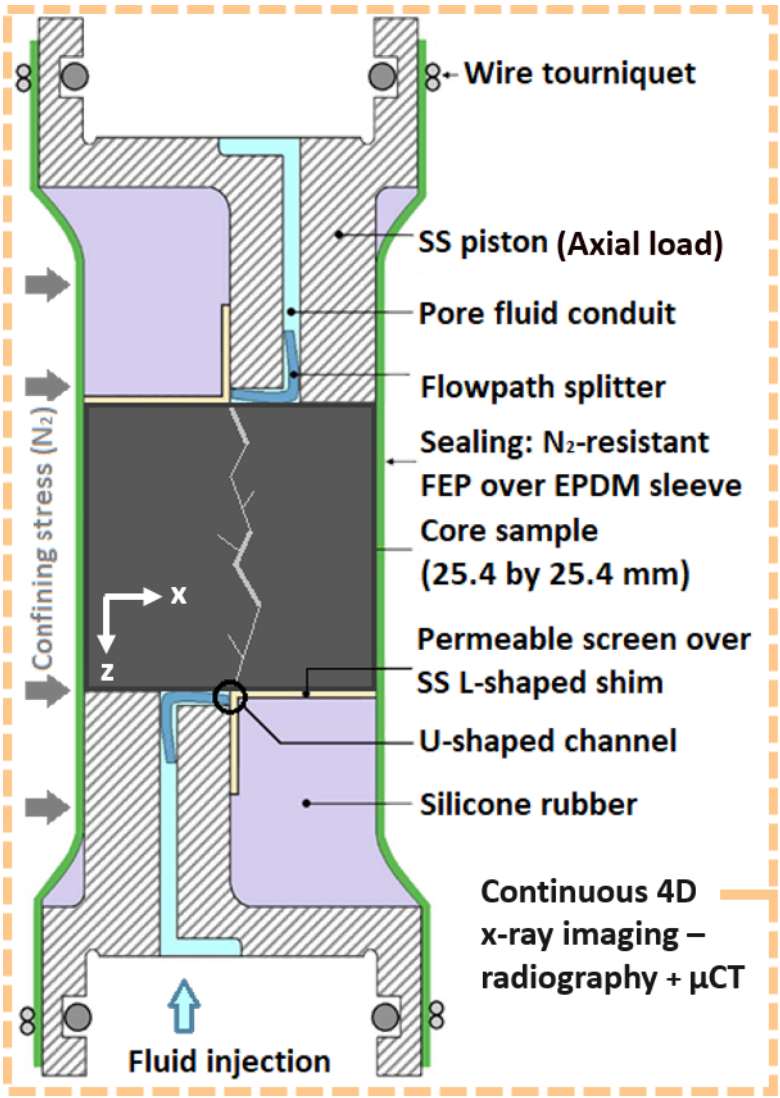

2019JB018864-f02-z-.tif

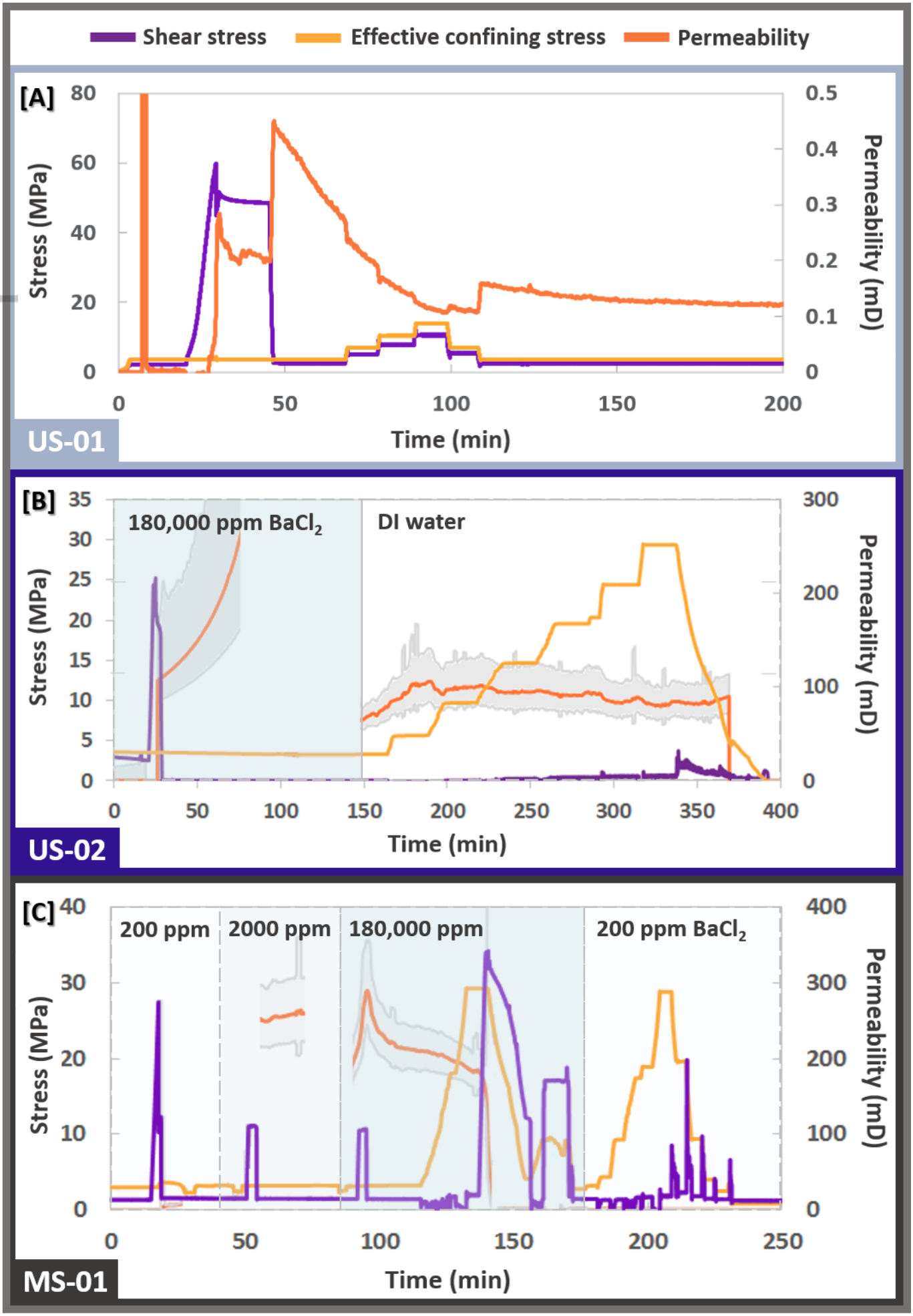

2019JB018864-f03-z-.tif

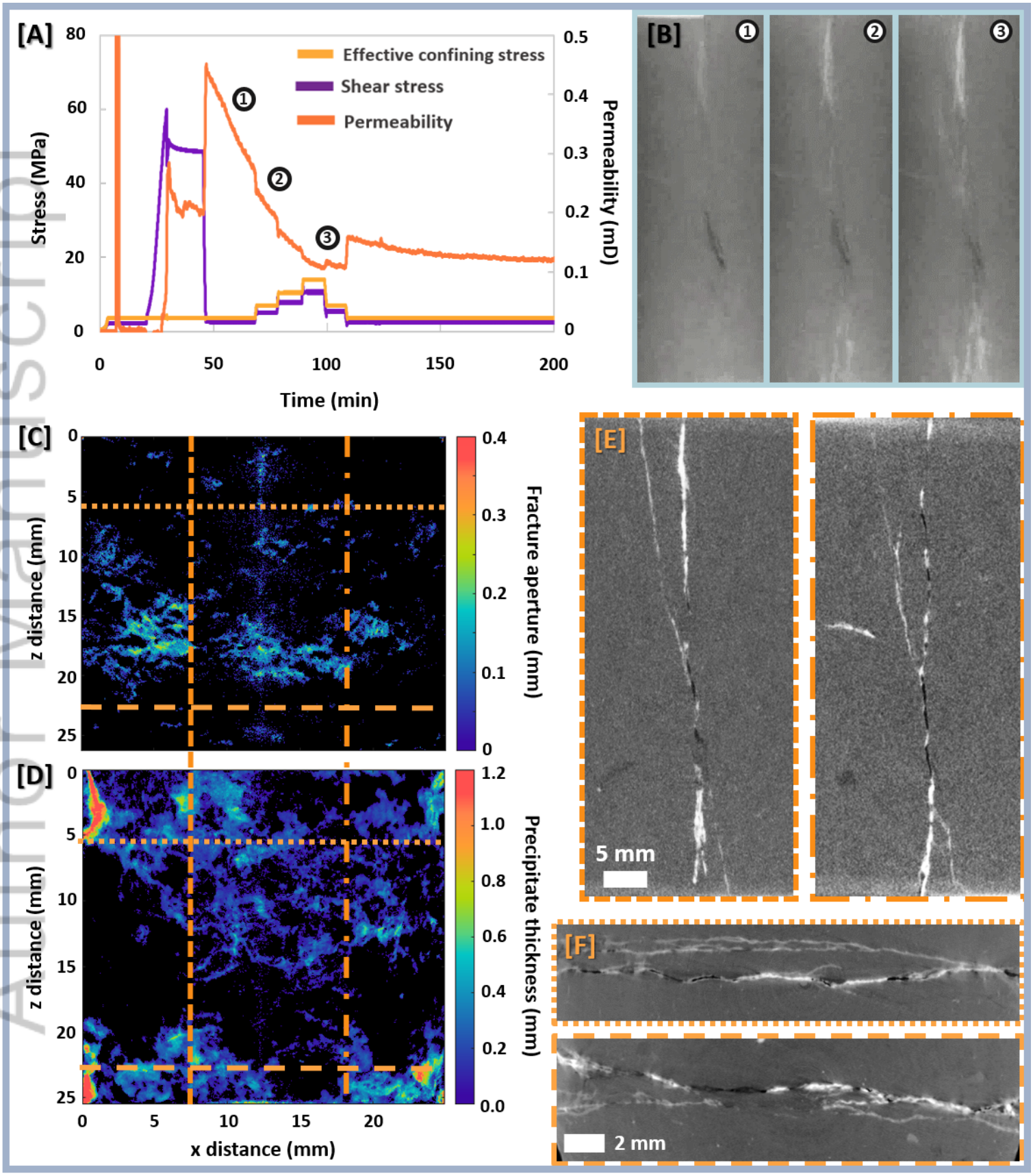

2019JB018864-f04-z-.tif

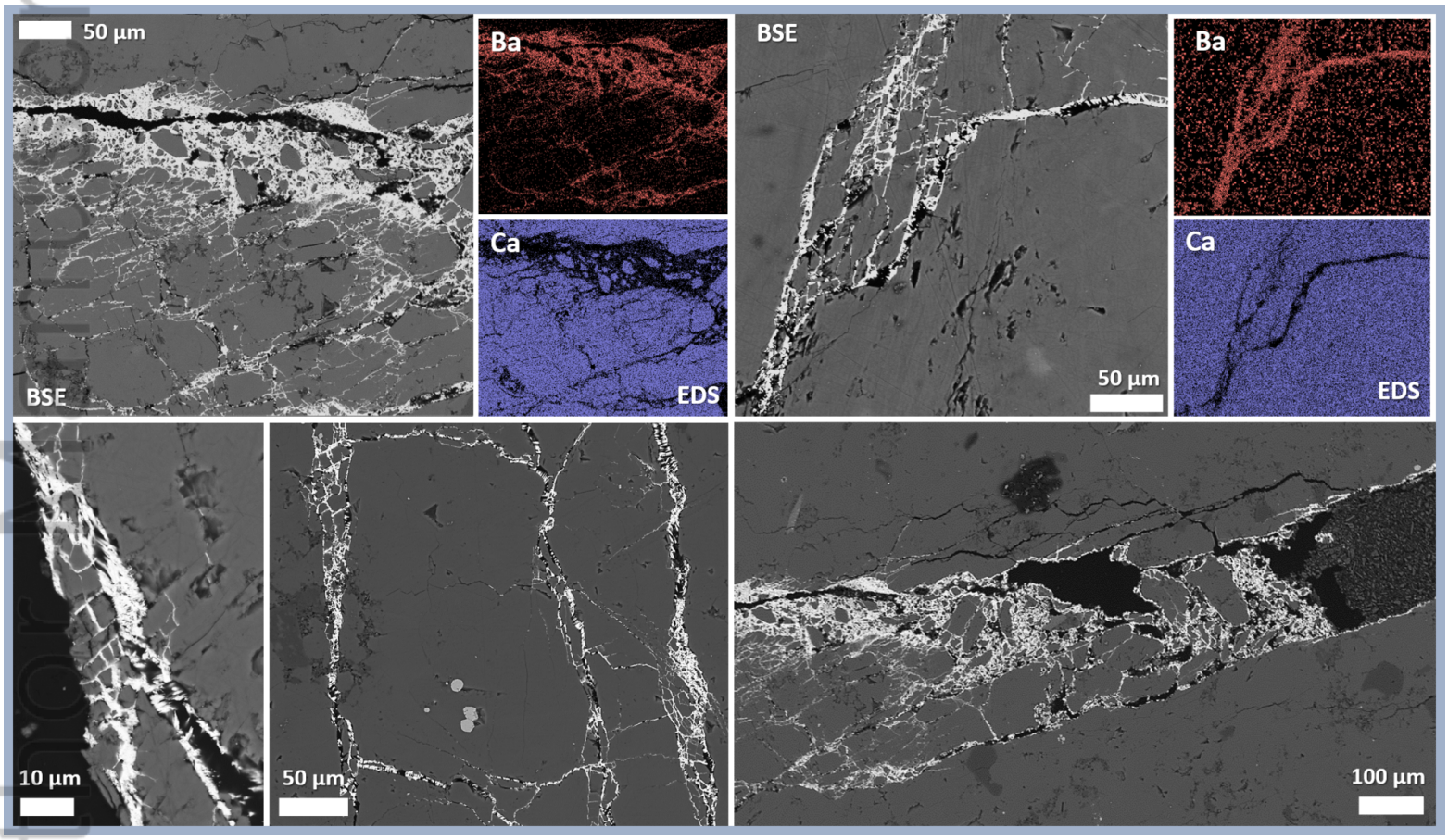

2019JB018864-f05-z-.tif

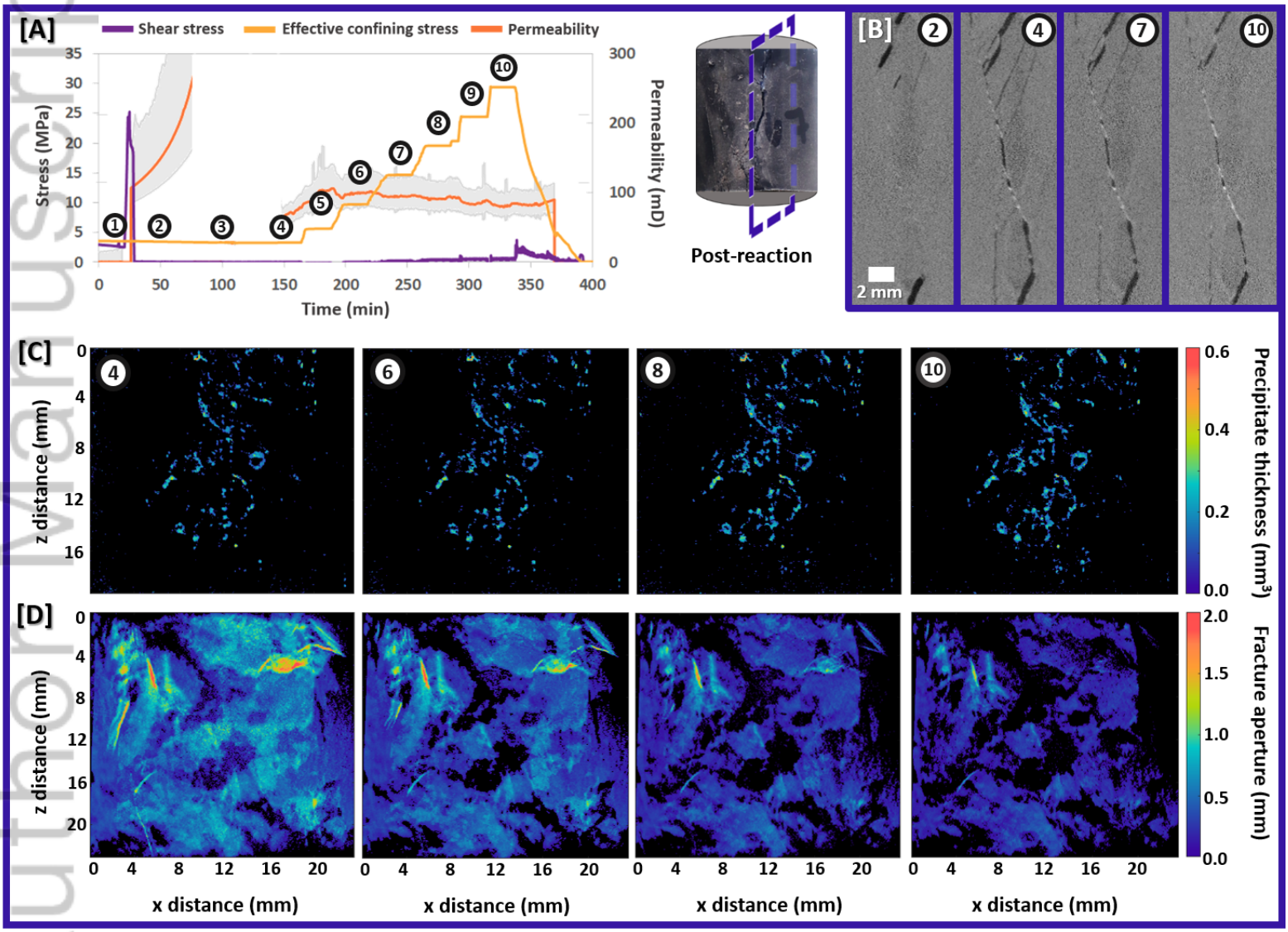

2019JB018864-f06-z-.tif

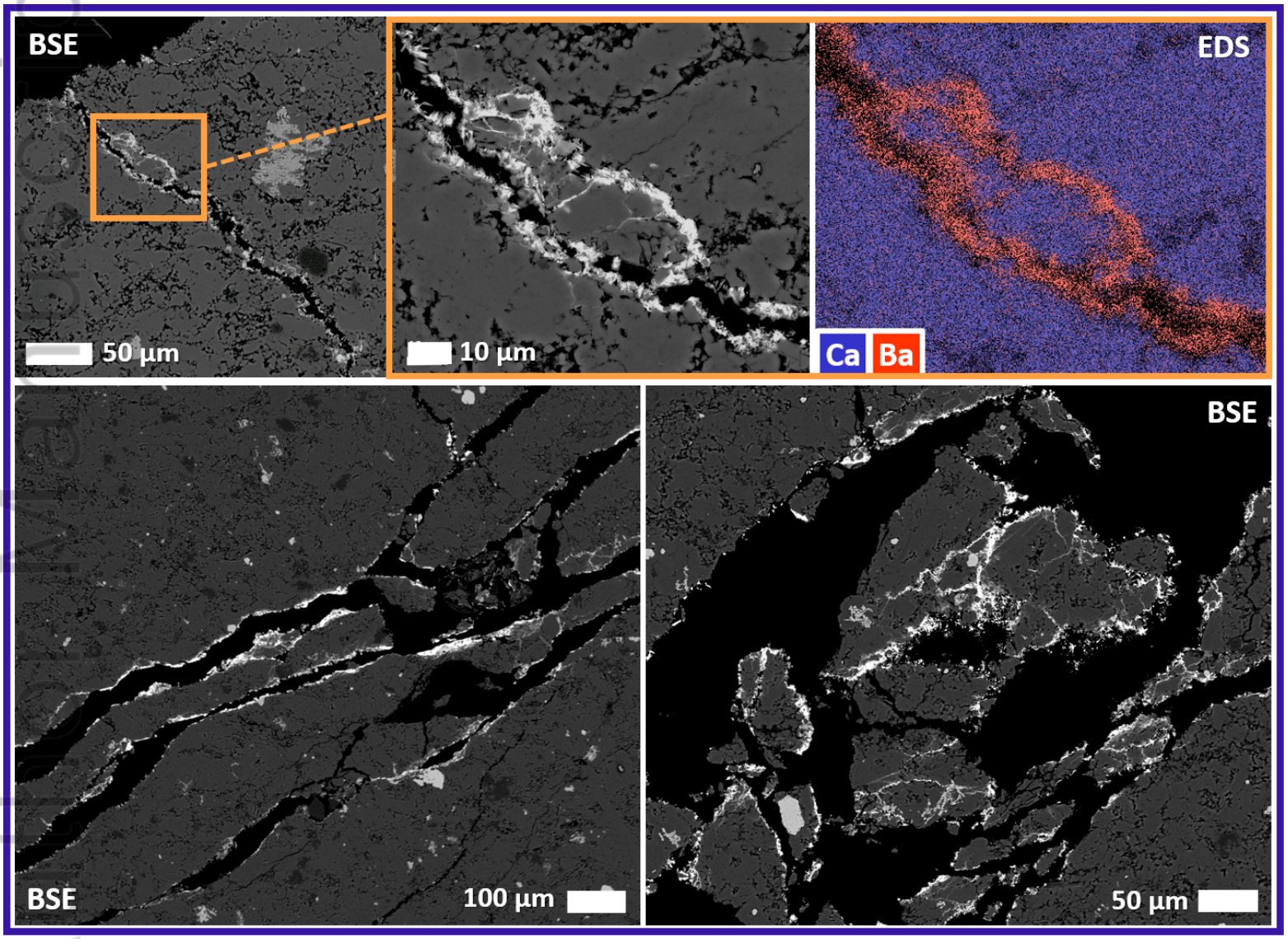

2019JB018864-f07-z-.tif

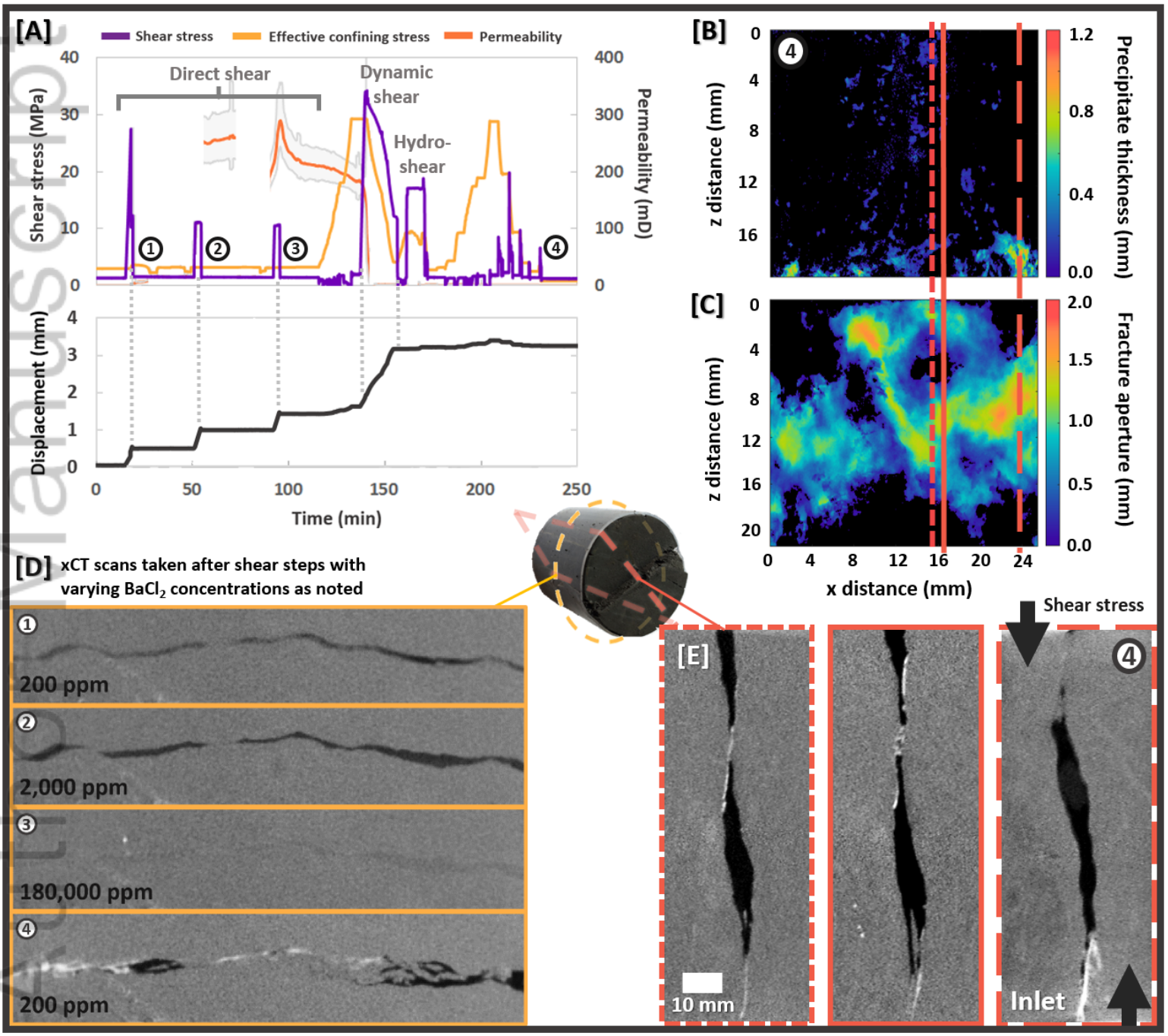

2019JB018864-f08-z-.tif

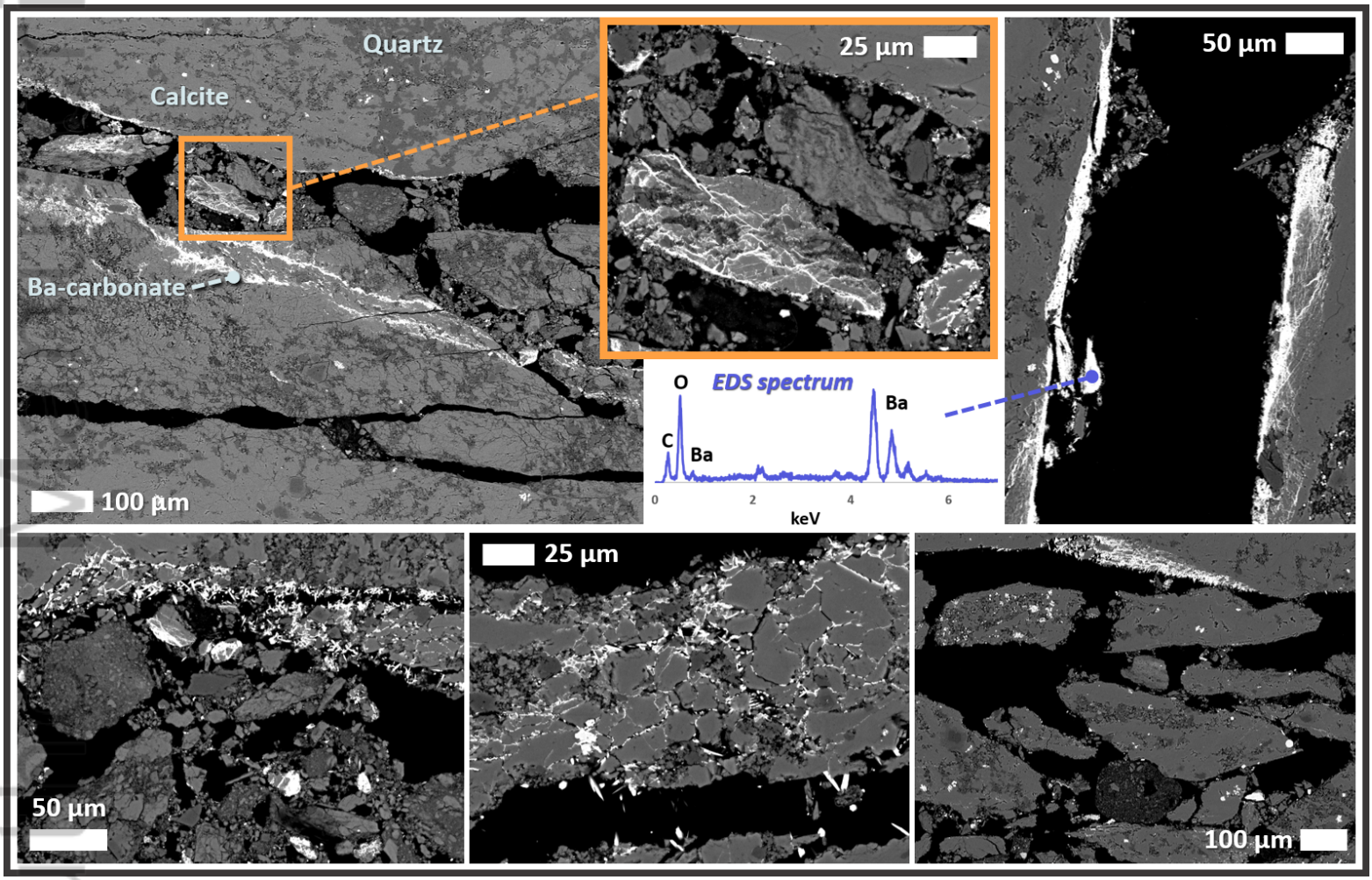

2019JB018864-f09-z-.tif

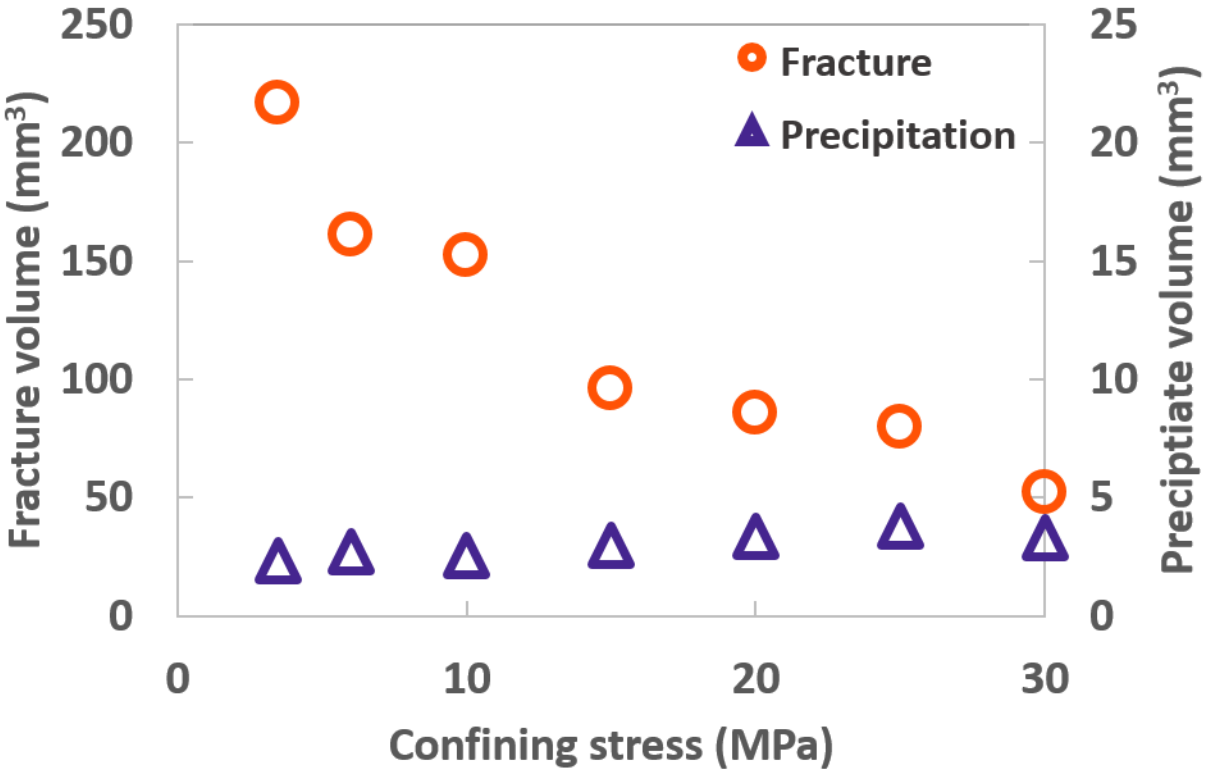

2019JB018864-f10-z-.tif